ANNUAL REVIEWS

Annual Review of Fluid Mechanics

Direct Numerical Simulation of Turbulent Flows Laden with Droplets or Bubbles

Said Elghobashi

Mechanical and Aerospace Engineering Department, University of California, Irvine, California 92689, USA; email: selghoba@uci.edu

Annu. Rev. Fluid Mech. 2019. 51:217–44

First published as a Review in Advance on September 5, 2018

The *Annual Review of Fluid Mechanics* is online at fluid.annualreviews.org

https://doi.org/10.1146/annurev-fluid-010518-040401

Keywords

direct numerical simulation, turbulent multiphase flows, droplets, bubbles

Abstract

This review focuses on direct numerical simulations (DNS) of turbulent flows laden with droplets or bubbles. DNS of these flows are more challenging than those of flows laden with solid particles due to the surface deformation in the former. The numerical methods discussed are classified by whether the initial diameter of the bubble/droplet is smaller or larger than the Kolmogorov length scale and whether the instantaneous surface deformation is fully resolved or obtained via a phenomenological model. Also discussed are numerical methods that account for the breakup of a single droplet or bubble, as well as multiple droplets or bubbles in canonical turbulent flows.

1. INTRODUCTION

Turbulent flows laden with liquid droplets or gas/vapor bubbles [known as a member of turbulent dispersed multiphase flows (TDMF), which include dispersed solid particles as well] are ubiquitous in nature and engineering applications. In nature, examples include rain, waterfall mists, air bubbles in the upper ocean, and vapor bubbles in geysers. Engineering applications include liquid fuel sprays in all types of combustion engines, paint sprays, spray drying in the pharmaceutical industry as well as food processing, and water vapor bubbles in nuclear reactor cooling systems or those created by cavitation in the wakes of ship propellers, just to list a few.

Direct numerical simulations (DNS) of TDMF are far more challenging than DNS of turbulent single-phase flows (TSPF). The reason is that TDMF possess, in general, a much wider spectrum of important length scales and timescales than that of TSPF. These scales are associated with the microscopic physics of the dispersed phase in addition to those of the carrier fluid, covering the range of fine to large structures of turbulence. Major advances in both supercomputer technologies and numerical methods during the past three decades have made it possible to perform DNS of TDMF at moderate Reynolds numbers. However, current and near-future parallel supercomputers do not allow the simultaneous resolution of all scales of TDMF, including the scales of motion around each of the millions of dispersed particles of size smaller than the finest scales of the carrier fluid motion.

Furthermore, DNS of turbulent flows laden with droplets or bubbles (the topic of the present review) are more challenging than DNS of solid-particle-laden turbulent flows due to the necessity of accounting for the shape deformation of the dispersed phase in the former.

Accurate prediction of the deformation of the interface between the dispersed and continuous phases requires proper accounting of the effects of surface tension and the different viscosities and densities of the two phases in the governing equations of motion. Two dimensionless quantities that measure the ability of the carrier fluid motion to deform the immersed droplets or bubbles are the Weber number, We, and the capillary number, Ca. We is the ratio of the inertial forces to surface tension forces, whereas Ca is the ratio of viscous forces to surface tension forces. Ca is used for droplets/bubbles whose size d is smaller than the Kolmogorov length scale, where the viscous forces are dominant compared to inertial forces. We is used when d is larger than the Kolmogorov length scale. Qualitatively, large values of We or Ca enhance the deformability whereas lower values reduce it.

The sizes of the droplets or bubbles in the studies reviewed here range from smaller to larger than the Kolmogorov length scale. In all the DNS studies reviewed, the governing conservation equations of the interacting fluid phases are solved on a fixed (Cartesian) grid. In other words, methods that use interface-fitting adaptive grids are not included in this review because these methods consider only nonturbulent flows.

Since current supercomputers allow DNS to resolve the turbulent fluid motion only at length scales greater than or equal to the Kolmogorov length scale, it is not possible at present to fully resolve the motion of dispersed deformable droplets or bubbles below the Kolmogorov scale. In order to overcome this difficulty, phenomenological models are used to compute the deformation of the dispersed phase, as discussed in Sections 2.1.2 and 3.1.2.

For deformable bubbles or droplets larger than the Kolmogorov length scale, the resolved shapes and motions of the interfaces between the two phases are computed via one of the following three approaches: tracking points, tracking scalar functions, or the immersed boundary method (IBM) with an interaction potential model (IPM).

According to the tracking points approach, the interface is marked by points that are advected by the flow, as in the front-tracking method (FTM) of Unverdi & Tryggvason (1992) and Tryggvason et al. (2001).

In the tracking scalar approach, each of the following four numerical methods has its tracking function:

1. For the volume of fluid (VOF) method, the relevant function is the volume fraction of the local phase on either side of the interface (Scardovelli & Zaleski 1999).
2. For the level set method, the function is the signed distance function representing the shortest distance from the interface (Sussman et al. 1994, Osher & Fedkiw 2001) or its hyperbolic-tangent version (Desjardins et al. 2008).
3. For the lattice Boltzmann method (LBM), the function is the probability density function, $f_i^n(\mathbf{x}, t)$, of finding a fluid particle of fluid phase n at position $\mathbf{x}$, at time t, and moving in the direction i of one of the discretized lattice velocity directions. The physical properties of the fluid, such as the density or momentum, are defined as moments of $f_i^n(\mathbf{x}, t)$. In discretized LBM, the moments are evaluated by quadrature summation over all i. The interface between two phases is modeled by adding an extra force to the lattice Boltzmann (LB) equilibrium velocity to represent the microscopic interaction between the two phases (e.g., surface tension or diffusivity) (Shan & Chen 1993).
4. For the phase field model (PFM), the function is the scalar phase field, $\phi(\mathbf{x}, t)$, also known as the order parameter, which represents one of the physical properties (e.g., molar concentration) of a binary fluid mixture. The function $\phi(\mathbf{x}, t)$ is mostly uniform in the bulk phases and varies smoothly over a diffuse interfacial layer of finite thickness. The transport of $\phi(\mathbf{x}, t)$ is governed by the Cahn–Hilliard equation (Cahn & Hilliard 1959), which accounts for the advection of $\phi(\mathbf{x}, t)$ by the fluid velocity and the diffusion, which equals $\nabla \cdot [M(\phi)\nabla\mu_\phi]$, where $M(\phi)$ is the fluid mobility and $\mu(\phi)$ is the chemical potential, which is defined in terms of the free energy $f(\phi)$ of the fluid. In contrast to the above methods 1–3, in PFM the surface tension forces are replaced by a continuum model of $f(\phi)$ (Jacqmin 1999). Accordingly, the Navier–Stokes equations are modified by adding the forcing function, $\mu\nabla\phi$, to represent the surface tension forces (Gurtin et al. 1996). Recently, a hybrid LBM-PFM was used to simulate the dispersion of liquid droplets in isotropic turbulence (Komrakova et al. 2015), as discussed in Section 3.2.4.

The recently developed hybrid IBM-IPM approach (Spandan et al. 2017a) couples IBM with a phenomenological IPM to simulate deformable droplets or bubbles in a turbulent flow. The dynamics of the interface deformation is modeled via a three-dimensional (3D) spring network distributed over the surface of the immersed droplet (de Tullio & Pascazio 2016). The IPM is based on the principle of minimum potential energy, where the total potential energy depends on the extent of the spring network's deformation. Modeling the spring network requires computing ad hoc elastic constants via a reverse-engineered approach. The IBM enforces the boundary conditions at the interface (e.g., the no-slip condition). A moving least squares (MLS) approximation (Vanella & Balaras 2009) is used to reconstruct the solution in the vicinity of the immersed surface and to convert the Lagrangian forcing back to the Eulerian grid. MLS ensures constructing uniform Lagrangian grid elements on the immersed surface as it deforms. Spandan et al. (2018) used the IBM-IPM approach to study the deformation of bubbles dispersed in a turbulent Taylor–Couette (TC) flow and the effect of their deformation on drag reduction. This study is discussed in Section 2.2.3.

Anderson et al. (1998) provided a historical review of the early studies by Poisson, Maxwell, Gibbs, Rayleigh, and van der Waals on modeling the interface between two immiscible fluids.

When necessary, the numerical methods are briefly discussed in this review. However, the focus here is not on the fine details of the different numerical algorithms but rather on the different methods' contributions to advancing our understanding of the physics of the interactions between

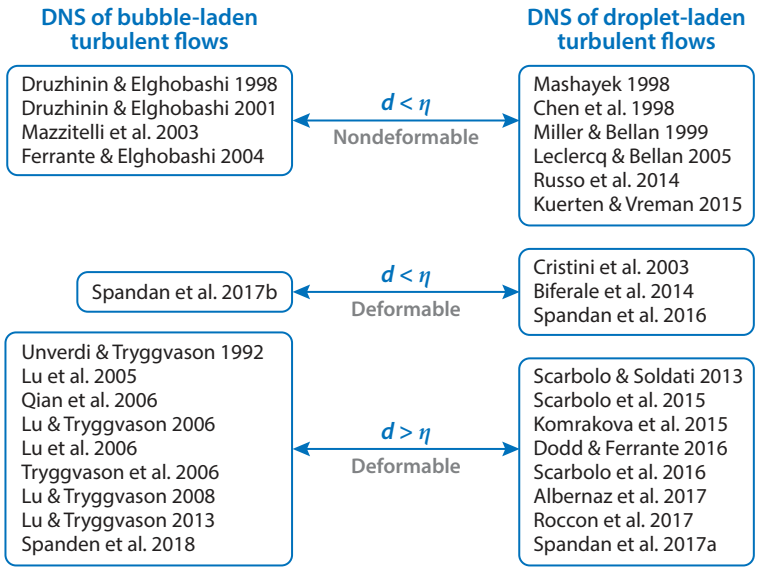

Figure 1

Direct numerical simulation (DNS) studies reviewed in this article of bubble- and droplet-laden turbulent flows for bubbles/droplets smaller ($d < \eta$) and larger ($d > \eta$) than the Kolmogorov length scale, η.

turbulence and droplets or bubbles. This review intends to complement the recent reviews of TDMF by Balachandar & Eaton (2010), of bubble-laden turbulent flows by Tryggvason et al. (2013), and of simulation methods of particulate flows by Maxey (2017).

The article proceeds as follows. Section 2 discusses DNS of bubble-laden turbulent flows, Section 3 discusses DNS of droplet-laden turbulent flows, and Section 4 provides concluding remarks.

2. DNS OF BUBBLE-LADEN TURBULENT FLOWS

The word "bubbles" in this review refers to either gas bubbles or vapor bubbles since the mechanical aspects of their motion in liquid are the same except for the stronger effects of added mass in the latter (Prosperetti 2017).

The length scale, d, is used in this review to denote the maximum size of the bubble. Thus, for a spherical bubble, d equals the diameter. For an ellipsoidal bubble, d equals the length of the major axis. In the following sections, the discussion considers bubbles whose size d is smaller than the Kolmogorov length scale, η, as well as bubbles with $d > \eta$. **Figure 1** shows a list of the authors whose papers are reviewed in this article.

2.1. Bubbles Smaller than the Kolmogorov Length Scale ($d < \eta$)

Bubbles of size $d < \eta$ are generally termed microbubbles (Madavan et al. 1984, Druzhinin & Elghobashi 1998). DNS of microbubble-laden turbulence can be performed using the two-fluid (TF) approach or the Eulerian–Lagrangian (EL) approach. The EL approach is based on the point particle assumption (Elghobashi & Prosperetti 2009, Balachandar & Eaton 2010).

2.1.1. Nondeformable spherical bubbles of size $d < \eta$. Following the approach of Maxey & Riley (1983), Druzhinin & Elghobashi (1998) derived the equation of motion of a nondeformable spherical microbubble of size $d < \eta$ in a turbulent flow, neglecting the Basset and lift forces and assuming $\rho_b \ll \rho_f$, where ρ_b and ρ_f are the densities of the bubble gas and surrounding fluid (liquid), respectively:

$$\frac{dV_i}{dt} = 3\frac{DU_i}{Dt} + \frac{1}{\tau_b}(U_{i,\mathbf{x}_b} - V_i + W\delta_{iz}), \quad 1.$$

where the bubble response time τ_b and terminal velocity W are defined as

$$\tau_b = \frac{d^2}{36\nu} \quad \text{and} \quad W = 2\tau_b g. \quad 2.$$

In the above equations, V_i and U_i are the instantaneous components of the bubble velocity and the carrier fluid velocity in the three coordinate directions (respectively), $\mathbf{x}_b$ is the position of the bubble center, $\frac{D}{Dt}$ is the Lagrangian derivative, g is the gravitational acceleration, and ν is the kinematic viscosity of the carrier fluid. Equation 1 is valid for the condition $d < \eta$, which simultaneously necessitates $\tau_b < \frac{\tau_K}{36}$ according to Equation 2, where τ_K is the Kolmogorov timescale. This condition on τ_b for the bubble does not have a corresponding restriction for the solid particle when using the equation of Maxey & Riley (1983), where the particle response time, τ_p, can be larger than τ_K.

Druzhinin & Elghobashi (1998) derived the TF equations for a bubble-laden turbulent flow by spatially averaging the governing equations of the carrier fluid and the bubble phase over a scale of the order of η, which is much larger than the bubble diameter. They used the TF equations to predict a bubble-laden Taylor–Green vortex flow and decaying isotropic turbulence with two-way coupling. The same authors used the TF equations in DNS to study a 3D bubble-laden spatially developing mixing layer with two-way coupling (Druzhinin & Elghobashi 2001).

Ferrante & Elghobashi (2007) performed DNS using the TF equations to study the effects of microbubbles on the vorticity dynamics in a Taylor–Green vortex flow. The results show that bubbles with a volume fraction of $\sim 10^{-2}$ enhance the decay rate of the vorticity at the center of the vortex. This is due to bubble clustering in the vortex core, which creates a positive velocity divergence. The vorticity transport equation shows that this positive $\nabla \cdot \mathbf{U}$ enhances the local vorticity decay.

To study drag reduction, Ferrante & Elghobashi (2004) performed DNS of a microbubble-laden spatially developing turbulent boundary layer over a flat plate at $Re_\theta = 1{,}430$. They included in Equation 1 the bubble lift force, $[(\mathbf{U} - \mathbf{V}) \times \boldsymbol{\Omega}_s]_i$, where $\boldsymbol{\Omega}_s$ is the local vorticity vector, in accordance with Auton (1987) and Auton et al. (1988). The lift force was needed for the bubble trajectories as they pass through the viscous sublayer where the fluid mean velocity gradient is maximum. The bubble diameter was $d_b = 62$ μm, $d_b^+ = 2.4$ in wall units, and the volume fraction Φ_v varied from 0.001 to 0.02. The authors concluded that

> the presence of bubbles [in the boundary layer] results in a *local* positive divergence of the fluid velocity, $\nabla \cdot \mathbf{U} > 0$, creating a positive mean velocity normal to (and away from) the wall which, in turn, reduces the mean streamwise velocity and displaces the quasi-streamwise longitudinal vortical structures away from the wall. This displacement has two main effects: (i) it increases the spanwise gaps between the wall streaks associated with the sweep events and reduces the streamwise velocity in these streaks, thus reducing the skin friction by up to 20.2% for $\Phi_v = 0.02$; and (ii) it moves the location of peak Reynolds stress production away from the wall to a zone of a smaller transverse gradient of the mean streamwise velocity (i.e., smaller mean shear), thus reducing the production rate of turbulence kinetic energy and enstrophy. (Ferrante & Elghobashi 2004, abstract, emphasis in original)

The drag reduction mechanism described above applies for nondeformable microbubbles of size $d < \eta$. Later we discuss that drag reduction can also be realized by deformable microbubbles (Section 2.1.2) and by deformable large bubbles of size $d > \eta$ (Section 2.2.2).

Mazzitelli et al. (2003) performed DNS of microbubble-laden isotropic turbulence using the point particle approach to study the two-way coupling effects, especially that of the lift force discussed above. They used 144,000 bubbles of size $d \sim 120$–250 μm and volumetric fraction $\Phi_v = 0.016$. However, they applied artificial forcing to the turbulence kinetic energy (TKE) spectrum, $E(k,t)$, at small wave numbers to create stationary turbulence at a fixed $Re_\lambda = 62$. This forcing camouflages the true two-way coupling effects of the bubbles on the flow, and thus no correct conclusion can be made about these effects. The camouflage is explained by the spectral transport equation of $E(k,t)$:

$$\frac{\mathrm{d}E(k,t)}{\mathrm{d}t} = T(k,t) - \varepsilon(k,t) + \Psi_b(k,t) + F(k,t), \qquad 3.$$

where the terms on the right-hand side are the transfer rate of TKE at wave number k, the dissipation rate, the bubbles' two-way coupling rate, and the artificial forcing rate, respectively. The instantaneous two-way coupling and transfer rates (after omitting the t) are

$$\Psi_b(k) = -\sum_{\kappa \le |\boldsymbol{\kappa}| < \kappa+1} \Re\left\{\left\langle \hat{u}_j^*(\boldsymbol{\kappa})\hat{f}_j(\boldsymbol{\kappa})\right\rangle\right\} \quad \text{and} \qquad 4.$$

$$T(\kappa) = \sum_{\kappa \le |\boldsymbol{\kappa}| < \kappa+1} \kappa_l P_{jk}(\boldsymbol{\kappa})\, \Im\left\{\sum_{\boldsymbol{\kappa}'} \left\langle \hat{u}_k(\boldsymbol{\kappa}')\hat{u}_l(\boldsymbol{\kappa}-\boldsymbol{\kappa}')\hat{u}_j^*(\boldsymbol{\kappa})\right\rangle\right\}, \qquad 5.$$

respectively, where $\Re\{\}$ and $\Im\{\}$ denote the real and imaginary parts,

$$P_{jk}(\boldsymbol{\kappa}) \equiv \delta_{jk} - \frac{\kappa_j \kappa_k}{\kappa^2} \qquad 6.$$

is the projection tensor, and δ_{jk} is Kronecker delta. $\hat{f}_j(\boldsymbol{\kappa})$ is the Fourier coefficient of the force f_j imparted by the bubbles on the surrounding fluid, and the asterisk (*) denotes the complex conjugate. The right-hand sides of both Equations 4 and 5 create nonlinear triadic interactions involving all wave numbers of $E(k,t)$, including the small wave numbers where $F(k,t)$ is applied (Ferrante & Elghobashi 2003). These triadic interactions are responsible for signaling the effects of the perturbations created by the microbubbles at high wave numbers to the large scales (small wave numbers) (Elghobashi & Truesdell 1993). Therefore, artificially increasing $E(k,t)$ at small wave numbers by $F(k,t)$ opposes the two-way coupling effects of the microbubbles. Furthermore, by definition, $\int_{k_{\min}}^{k_{\max}} \frac{\mathrm{d}E(k,t)\mathrm{d}k}{\mathrm{d}t} = \frac{\mathrm{d}E}{\mathrm{d}t} = 0$ for a forced stationary turbulence, and thus an invariant $E(t)$ cannot show any effects of the two-way coupling. It is important to note that it is appropriate to use forced isotropic turbulence to study the dispersion of bubbles or particles in one-way coupling (e.g., Wang & Maxey 1993, Snyder et al. 2007).

The word "artificial" in the above discussion distinguishes between the definition of homogeneous isotropic turbulence (used by Taylor and Kolmogorov), in which the production of TKE is zero because of the statistical correlations $\langle u_i u_j \rangle = 0$ for $i \neq j$, and that of shear flows (jets, wakes, and channel flows), in which TKE is produced naturally by the interactions between finite $\langle u_i u_j \rangle$ and gradients of mean velocities. In forced isotropic homogeneous turbulence, the TKE is added artificially to the flow since no natural production of TKE exists.

2.1.2. Deformable bubbles of size $d < \eta$. Performing DNS of TDMF to resolve the shape deformation of millions of bubbles or droplets with $d < \eta$ is beyond the capabilities of current

parallel supercomputers. For example, performing DNS of isotropic homogeneous TSPF at $Re_\lambda = 500$ in a cubical domain requires a mesh of $N^3 = 2{,}048^3 \simeq 8.6 \times 10^9$ points. A typical value of the Kolmogorov length scale for that flow is $\eta \simeq 5 \times 10^{-4}$ m. Assume that 80×10^6 liquid droplets of diameter $d = 5 \times 10^{-5}$ m at a volume fraction of $\Phi_v = 10^{-3}$ are being dispersed in that flow. Now, performing DNS to resolve the flow inside and outside each of these droplets would require at least 20 mesh points per droplet diameter in each of the three coordinate directions. Since we have $d/\eta = 0.1$, the mesh side length Δ of each of the $2{,}048^3$ cells has to be subdivided into 200 divisions. In other words, the cubical domain would require $(200 \times 2{,}048)^3 \simeq 69 \times 10^{15}$ mesh points. Furthermore, the time step for this TDMF would be smaller by a factor of 200 compared to that of the above-described TSPF. No current or near-future supercomputer would be capable of performing these computations. However, it is feasible to use the point particle approach combined with a phenomenological subgrid model to calculate the shape deformation of the dispersed phase. The study by Spandan et al. (2017b) was the first (and presently only) study that followed that approach and thus is described here in some detail. Spandan et al. (2017b) performed DNS to study the flow of deformable sub-Kolmogorov bubbles dispersed in a turbulent TC flow. They used a two-way coupled point particle approach and were able to simulate approximately 10^5 continuously deforming bubbles. The density ratio $\hat{\rho}$ of the bubble gas density to that of the liquid was 10^{-3}, the viscosity ratio $\hat{\mu}$ was 10^{-2}, and the volume fraction Φ_v of the bubbles was 10^{-3}. The study focused on the effect bubble deformability had on the reduction of the torque required to rotate the inner cylinder at a prescribed angular velocity. The reduction of the required torque is calculated by comparing the average shear stress at the rotating wall for the bubble-laden flow with that of a single-phase flow. The rotation rate of the inner cylinder was quantified by the inner cylinder Reynolds number, $Re_i = r_i\omega_i(r_o - r_i)/\nu$, where r_i, r_o, ω_i, and ν are the inner cylinder radius, outer cylinder radius, inner cylinder angular velocity, and the kinematic viscosity of the carrier fluid, respectively. Two cases were simulated with $Re_i = 2.5 \times 10^3$ and 8×10^3.

The bubble shape was assumed to be at all times a triaxial ellipsoid described by a symmetric, positive definite, second-rank tensor $\mathbf{S}$ satisfying the condition $\mathbf{S}^{-1}$: $\mathbf{xx} = 1$, where $\mathbf{x}$ is the position vector of any point on the ellipsoid surface relative to its center. The time rate of change of $\mathbf{S}$ is described by the phenomenological equation of Maffettone & Minale (1998), which was originally developed for liquid droplets,

$$\frac{\mathrm{d}\mathbf{S}}{\mathrm{d}t} - (\mathbf{\Omega}\cdot\mathbf{S} - \mathbf{S}\cdot\mathbf{\Omega}) = -\frac{f_1}{\tau}\Big(\mathbf{S} - \mathrm{g}(\mathbf{S})\mathbf{I}\Big) + f_2\Big(\mathbf{E}\cdot\mathbf{S} + \mathbf{S}\cdot\mathbf{E}\Big), \qquad 7.$$

where $\tau = \mu R/\sigma$ is the interfacial timescale, μ is the dynamic viscosity of the carrier fluid (liquid), R is the radius of the equivalent undeformed spherical bubble, and σ is the surface tension. $\mathbf{E}$ and $\mathbf{\Omega}$ are the strain rate and rotational rate tensors, respectively. $\mathbf{I}$ is the second-rank unit tensor.

The left-hand side of Equation 7 is the Jaumann corotational derivative (Gurtin et al. 2010), which is frame invariant and depends on $\mathbf{\Omega}$. Equation 7 states that the temporal evolution of the shape tensor is governed by two competing phenomena: the interfacial tension (the first term on the right-hand side), which attempts to restore the initial spherical shape, and the drag exerted by the motion of the ellipsoid while preserving the initial volume (the second term on the right-hand side). The positive dimensionless coefficients f_1 and f_2 are functions of the viscosity ratio $\hat{\mu}$. The function g($\mathbf{S}$) is introduced to preserve the bubble volume and is proportional to the ratio of the third invariant of $\mathbf{S}$ to the second invariant of $\mathbf{S}$. The derivation of Equation 7 is given by Maffettone & Minale (1998).

Time integration of Equation 7 leads to three eigenvalues of $\mathbf{S}$, which equal the squares of the three semiaxes of the ellipsoid, and three eigenvectors, which provide the orientations of the

semiaxes. Equation 7 has been validated experimentally by Guido et al. (2000) for a neutrally buoyant liquid droplet immersed in a viscous fluid subjected to uniform shear. Spandan et al. (2017b) assumed a small capillary number, which measures the relative importance of the viscous forces to surface tension forces at the small-scale motion, i.e., $Ca = \tau/\tau_K = (\eta\,\mu_f)/(\sigma\,\tau_K) \ll 1$, where μ_f is the dynamic viscosity of the carrier fluid and τ_K is the Kolmogorov timescale.

To ensure that the deformed ellipsoidal bubble is nearly axisymmetric, Spandan et al. (2017b) further assumed that $Ca_{max} = 0.1$. To satisfy the no-slip boundary condition, they used the drag and lift coefficients developed by Njobuenwu & Fairweather (2015) for solid ellipsoidal particles by assuming that the bubble interface is contaminated with surfactants. D. Lohse (personal communication) justified using the no-slip boundary condition for the bubble surface and the drag and lift forces for solid ellipsoids by setting $Ca \ll 1$ and $\hat{\mu} = 10^{-2}$; hence, the viscosity of the bubble gas was negligible, thus minimizing the drag due to the internal gas circulation. The bubble acceleration equation accounted for the forces due to drag, lift, added mass, and buoyancy. It should be noted that whether the interface of a bubble or droplet is clean or contaminated (e.g., with surfactants) has significant effects on its shape deformation and motion dynamics (e.g., drag and lift forces) and, consequently, on the mathematical/numerical treatment of the boundary conditions at the interface (Clift et al. 1978).

The DNS results show that an increase in the deformability of the sub-Kolmogorov bubbles enhances drag reduction due to a significant accumulation of the deformed bubbles near the rotating inner wall (**Figures 2** and **3**). In **Figure 2**, the dimensionless deformation parameter is $D = (d_3 - d_1)/(d_3 + d_1)$ (Maffettone & Minale 1998), where d_1 and d_3 are the lengths of the minor and major semiaxes of the ellipsoid, respectively. A larger concentration of bubbles near the driving wall indicates that they are effective in suppressing the plumes' ejection process; hence, drag reduction is greater. These plumes are unsteady vortical structures that detach from either the inner or outer cylinder in the wall-normal direction (van der Veen et al. 2016). The plume ejection occurs predominantly at the stagnation regions (along the walls) between the

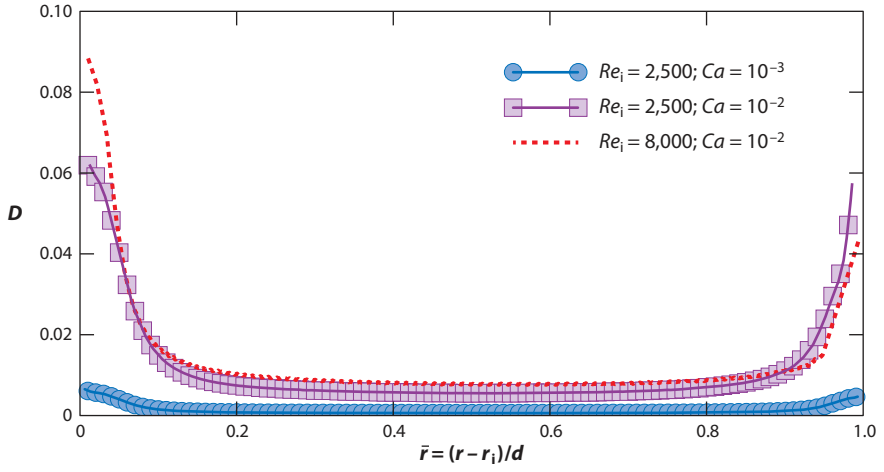

Figure 2

Radial (wall-normal) profiles of azimuthally, axially, and temporally averaged deformation parameter D of the sub–Kolmogorov length scale bubbles for two capillary numbers, with inner cylinder Reynolds number $Re_i = 2{,}500$ and 8,000. Figure adapted from Spandan et al. (2017b) with permission from the American Physical Society.

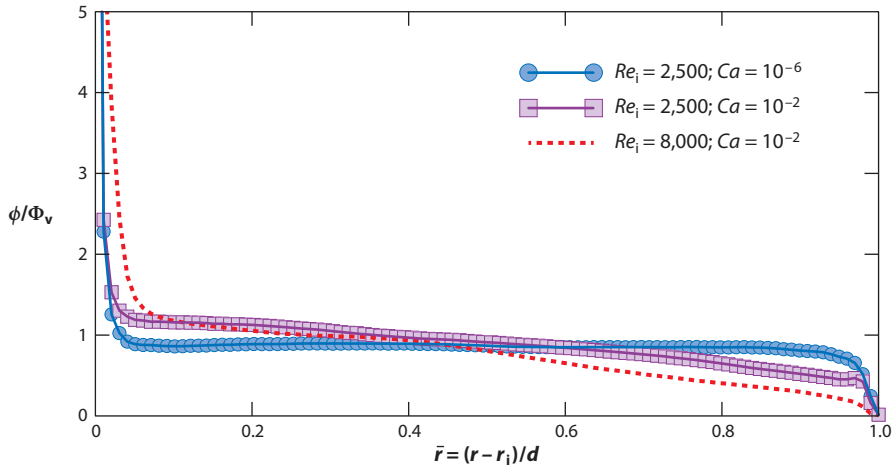

Figure 3

Radial (wall-normal) profiles of azimuthally, axially, and temporally averaged local volume fraction, ϕ, of the sub–Kolmogorov length scale bubbles, normalized by the total volume fraction, Φ_v, for two capillary numbers, with inner cylinder Reynolds number $Re_i = 2{,}500$ and 8,000. Figure adapted Spandan et al. (2017b) with permission from the American Physical Society.

counter-rotating rollers where a negative pressure gradient normal to the wall is created. The bubbles' preferential accumulation is induced by increased resistance to the bubbles leaving the wall in its normal direction. The increased resistance is due to the strong deformation of the bubbles near the rotating wall, which makes them prolated (stretched along one axis) and oriented along the streamwise direction.

2.2. Bubbles Larger than the Kolmogorov Length Scale ($d > \eta$)

In the following three subsections, we review studies of bubble deformation in isotropic turbulence using LBM, as well as in turbulent channel flow using FTM, and in turbulent TC flow using IBM-IPM.

2.2.1. Single-bubble deformation and breakup in isotropic turbulence using the lattice Boltzmann method. Qian et al. (2006) studied the deformation and breakup of a single bubble in stationary isotropic turbulence ($20 \leq Re_\lambda \leq 35$) using LBM with a D3Q15 lattice (see Section 3.2.1) and the BGK (Bhatnagar–Gross–Krook; Bhatnagar et al. 1954) form of the LB equation with single relaxation time. A validation test was made for a nonturbulent flow by comparing the results of this LBM with those of FTM for a 2D rising bubble and showed good agreement (Sankaranarayanan et al. 2003). Qian et al. (2006) defined the Weber number as $We = \rho_l \langle \delta u^2 \rangle d_e/\sigma$, where δu is the velocity difference over a distance equal to the bubble's equivalent spherical diameter, d_e, and the angle brackets denote averaging over space and time. The results show that, prior to the bubble breakup, the bubble surface area increases by at least 37%. They compared their results with the experimental data of Risso & Fabre (1998), which were conducted in a microgravity environment. Both the experiment and LBM indicate that there is a Weber number below which breakup is not observed. This Weber number is based on the statistics of the single-phase flow that would exist in the absence of the bubble. In LBM, this Weber number was approximately 3.0.

2.2.2. Deformable bubbles of size $d > \eta$ in turbulent channel flow using the front-tracking method. Unverdi & Tryggvason (1992) introduced FTM, in which one set of the incompressible Navier–Stokes and continuity equations is used for the whole computation domain, including the bubbles and the carrier liquid:

$$\rho\frac{\partial \mathbf{u}}{\partial t} + \rho\nabla\cdot\mathbf{uu} = -\nabla P + \nabla\cdot\mu(\nabla\mathbf{u} + \nabla\mathbf{u}^T) + \sigma\int_F k_f\,\mathbf{n}_f\,\delta(\mathbf{x}-\mathbf{x}_f)\,dA_f, \quad 8.$$

$$\nabla\cdot\mathbf{u} = 0, \quad 9.$$

where $\mathbf{u}$ is the velocity, P is the pressure, ρ and μ and are the discontinuous density and viscosity fields, respectively, δ is a 3D delta function, σ is the surface tension coefficient, k is twice the mean curvature, the subscript f denotes the front, $\mathbf{n}_f$ is a unit vector normal to the front, $\mathbf{x}$ is the point at which the equation is solved, and $\mathbf{x}_f$ is the position of the front. The integral is over the entire front such that it creates a force that acts at the interface but is smooth along the front.

The moving interface (front) between the bubble gas and the surrounding liquid is represented by an unstructured mesh that explicitly marks the position of the front. The front mesh (or marker) points are advected by the carrier flow velocities, interpolated from the fixed Cartesian mesh. As the front deforms, surface markers are dynamically added or removed. An indicator function, $\mathbf{I}(\mathbf{x})$, which has the value 1 inside the bubble and 0 in the carrier liquid, is constructed from the known position $\mathbf{x}_f$. Since both ρ and μ are constant within each fluid, their values at any point can be calculated using $\mathbf{I}(\mathbf{x})$ via the equations $\rho(\mathbf{x}) = \rho_0 + (\rho_b - \rho_0)\mathbf{I}(\mathbf{x})$ and $\mu(\mathbf{x}) = \mu_0 + (\mu_b - \mu_0)\mathbf{I}(\mathbf{x})$, where the subscripts b and 0 denote the bubble and carrier fluids, respectively.

The front is given a thickness of the order of several mesh cells to avoid numerical instabilities associated with a sharp interface. In this narrow transition zone, the fluid properties change smoothly. The sharp delta functions in Equation 8 are approximated by smoother functions with a compact stencil on the fixed Cartesian mesh. At each time step, after the front has been advected, the density and the viscosity fields are reconstructed by integration of the smooth grid delta function. The surface tension force (the last term on the right-hand side of Equation 8) is then added to the nodal values of the discretized Navier–Stokes equations. More details are given by Tryggvason et al. (2006).

Lu et al. (2005) performed DNS of a turbulent flow in a minimum channel at $Re_\tau = 135$. They used the FTM described above to study the effect of 16 dispersed bubbles on the wall shear stress. The nondeformed bubble diameter was 54 wall units. The density ratio was restricted to $\rho_b/\rho_0 = 0.1$, and the dynamic viscosity ratio was fixed at $\mu_b/\mu_0 = 1$, which resulted in a kinematic viscosity ratio $\nu_b/\nu_0 = 10$, a typical value for air bubbles in liquid water. Three Weber numbers were tested: 0.203, 0.270, and 0.405. The results show that deformable bubbles (with largest We) can lead to a significant reduction of the wall drag by suppression of streamwise vorticity. Less deformable bubbles, however, are slowed down by the viscous sublayer and lead to a large increase in drag. The reduction of streamwise vorticity occurs by bubbles moving parallel to the wall at a distance of about one bubble radius between the bubble surface and the wall. These bubbles move over the streamwise vortices with a higher velocity than the advection velocity of the vortices. The bubbles' passing forces the streamwise vortices closer to the wall, causing the streamwise vortices and the wall-bounded vorticity of the opposite sign to mutually cancel out. This reduces the streamwise vorticity and correspondingly the $\overline{uv}$ component of the Reynolds stress tensor. Tryggvason et al. (2006) discussed the numerical difficulties that arise when using FTM with large density and viscosity ratios.

Lu & Tryggvason (2006) performed DNS with FTM to study a bubbly vertical channel downflow at friction Reynolds number $Re_\tau = 127$. The number of bubbles ranged from 18 to 72, with an average volume fraction Φ_v ranging from 0.015 to 0.06 and a diameter of $0.25H$, where H

is half of the channel width. The density and kinematic viscosity ratios were $\rho_b/\rho_0 = 0.1$ and $\nu_b/\nu_0 = 10$, respectively. The results show that the lift force on the bubbles near the wall caused them to concentrate in the core region and create a bubble-free wall layer.

Lu & Tryggvason (2008) performed DNS with FTM to study the effect of deformability of 21 bubbles on their dispersion in a turbulent bubbly upflow in a vertical channel at friction Reynolds number $Re_\tau = 127$. The density and viscosity ratios were prescribed as those in Lu & Tryggvason (2006). Two cases were studied for two values of the Eötvös number, $Eo = \rho_f g d^2/\sigma$, which measures the ratio of gravitational forces to surface tension forces: 0.45 for nearly spherical bubbles and 4.5 for deformable bubbles. The lift force on a clean spherical bubble rising in a vertical shear flow is directed toward the side where the fluid moves faster past the bubble in a frame of reference moving with the bubble (Lu et al. 2006), according to Saffman (1965). In channels, where the fluid velocity is zero at the walls, spherical bubbles therefore move laterally toward the walls in upflow and away from the walls in downflow. However, bubble deformation can reverse the sign of the lift force. Furthermore, the lift force on strongly deformable bubbles is weaker than that on nearly spherical bubbles. Turbulent dispersion of deformable bubbles overcomes their tendency to concentrate in the core region of this upflow.

Lu & Tryggvason (2013) performed DNS of nearly spherical bubbles in a vertical turbulent channel upflow similar to their earlier study (Lu & Tryggvason 2008) but at higher Reynolds number ($Re_\tau = 250$) and with 140 bubbles. The bubble diameter was prescribed to be 40 wall units, or 8% of the channel width. At a statistically steady state, the weight of the bubble-laden liquid and the imposed pressure gradient are balanced by the shear stress. For the upflow in the channel, as the bubbles migrate toward the wall (by the lift force), the average mixture density in the core increases until the weight is balanced exactly by the pressure gradient. The shear force, and subsequently the lift force, vanish in the core region, thus ending the bubbles' migration to the wall. As a result, the velocity gradient exists only in the wall region where the bubbles' volume fraction reaches its peak (see Lu & Tryggvason 2013, figures 3 and 4). The high concentration of bubbles in the wall layer results in a significant reduction of the TKE and its dissipation rate there. However, figure 5 of Lu & Tryggvason (2013) also shows that the peak of the dissipation rate increases very close to the wall as compared to single-phase flow, for reasons that were not discussed.

2.2.3. Deformable bubbles of size $d > \eta$ in turbulent Taylor–Couette flow using the immersed boundary method with the interaction potential model. Spandan et al. (2018) performed DNS to study the effects of dispersed deformable bubbles of size $d > \eta$ on drag reduction in a turbulent TC flow using hybrid IBM-IPM (see Section 1). The surface of each dispersed bubble was discretized using an unstructured Lagrangian mesh. The effect of the bubbles on the carrier fluid was accounted for via a volume-averaged force that is computed on that mesh and then transferred to the Eulerian mesh where the NS equations are solved. The deformation of the immersed bubbles is computed via the IPM, where the surface tension of a liquid–gas interface is modeled using a triangulated network of elastic and torsional springs, as described by Spandan et al. (2017a). Two cases were simulated with inner cylinder Reynolds numbers, 5×10^3 and 2×10^4. The number of the dispersed bubbles was 120, each with an initial diameter of $d_b \sim 14\eta$ and $d_b \sim 25\eta$ for the low- and high-Re_i cases, respectively, and the global volume fraction Φ_v was 0.001. Each bubble was initialized as a sphere with its surface discretized with 1,280 and 2,560 Lagrangian marker points for the low- and high-Re_i cases, respectively. Four values of Weber number, based on the velocity of the inner cylinder, were considered: 0.01, 0.5, 1, and 2. These values were assumed to be small enough to avoid bubble breakup. The ratio, $\hat{\rho}$, of the bubble gas density to that of the liquid was 5×10^{-2}. Bubble–bubble and bubble–wall collisions

were modeled via an elastic potential between the Lagrangian mesh nodes and the center of the enclosing Eulerian cell.

The results show that for all four *We* values, the bubbles concentrate near the inner cylindrical wall. This is in contrast to the deformable sub-Kolmogorov bubbles that preferentially concentrate near the inner wall as *Ca* is increased (see Section 2.1.2).

Sugiyama et al. (2008) derived the drag reduction of the bubble-laden TC flow as the sum of two terms, $DR_1 = \left(1 - \frac{\langle \varepsilon_B \rangle}{\langle \varepsilon \rangle}\right)$ and $DR_2 = \left(\frac{\langle \mathbf{f}_b \cdot \mathbf{u} \rangle}{\langle \varepsilon \rangle}\right)$, where $\langle \varepsilon_B \rangle$ and $\langle \varepsilon \rangle$ are the mean dissipation rates of TKE per unit mass of the bubble-laden carrier fluid and the single-phase flow, respectively. The volume-averaged source term in the Navier–Stokes equations, $\mathbf{f}_b$, represents the two-way force per unit mass of the carrier flow due to the dispersed bubbles, and $\mathbf{u}$ is the local fluid velocity. The results show that DR_1 dominates DR_2 and increases with increasing *We*. The reason is that when the bubbles are more deformable, they are stretched along the streamwise direction similar to that of sub-Kolmogorov deformable bubbles (see Section 2.1.2). The stretching reduces the projected surface area in the direction of the relative velocity, which in turn lowers the bubble Reynolds number, leading to smaller wake, lower TKE, and thus smaller $\langle \varepsilon_B \rangle$ and lower DR_1.

3. DNS OF DROPLET-LADEN TURBULENT FLOWS

3.1. Droplets Smaller than the Kolmogorov Length Scale ($d < \eta$)

Examples of liquid droplets of diameter $d < \eta$ include rain droplets in the atmospheric boundary layer and fuel droplets in the combustion chambers of modern aircraft jet engines. Carl et al. (2001) measured the size distribution of the liquid fuel droplets under realistic conditions in the combustion chamber of an aircraft jet engine, and their data show that the diameter of most droplets is smaller than η in the region downstream of the initial ligament breakup zone.

3.1.1. Nondeformable droplets of size $d < \eta$. Mashayek (1998) performed DNS with the point particle approach and 96^3 grid points to study droplet–turbulence interactions in a homogeneous shear flow. He considered both one-way and two-way couplings for nonevaporating and evaporating droplets. The number of droplets was 1.5×10^5, and the diameter of nonevaporating droplets varied between 0.2η and 0.3η. The study showed that in the case of nonevaporating droplets, the TKE is reduced and the flow anisotropy is increased due to the two-way coupling. In the case of evaporating droplets, he found that the TKE and the mean internal energy of the carrier flow are increased due to the mass transfer of the droplet vapor to the carrier fluid.

Chen et al. (1998) studied the collision and coalescence of mono-sized droplets in a turbulent channel using DNS with the point particle approach at friction Reynolds number $Re_\tau = 116$. The droplet diameter ranged from 0.1η to 0.5η, and the initial volume fraction was in the range $5.8 \times 10^{-6} \leq \Phi_v \leq 3.1 \times 10^{-4}$. The ratio of the liquid density to that of the carrier fluid varied from 20 to 2,000. The results showed that the droplet inertia was the dominant factor in the collision mechanism. The results also showed that the predicted collision rate agreed with the theory of Saffman & Turner (1956) for droplets with a response time in wall units of $\tau_d^+ < 1$.

Miller & Bellan (1999) performed DNS of a confined temporally developing mixing layer with one layer laden with evaporating liquid droplets using the point particle approach and two-way coupling for mass, momentum, and energy exchanges. The confining walls were treated as frictionless and adiabatic to simplify the boundary conditions for the droplets and ensure the

conservation of mass and energy. The initial volume fraction of the droplets in the laden stream was 5.5×10^{-4}. The initial number of the mono-size droplets in the different cases varied from 4×10^4 to 7.3×10^5, and their initial diameter ranged from 115 to 231 μm. The Reynolds number based on the vorticity thickness was 200, and the convective Mach number M_c was 0.5. The initial temperatures of the gas and droplets were 350 K and 325 K, respectively. The results show that the TKE and the growth rate of the mixing layer were both attenuated monotonically by increasing the mass loading ratios of the droplets.

Leclercq & Bellan (2005) extended the mathematical formulation of Miller & Bellan (1999) to account for multicomponent chemical composition of the liquid droplets. They examined the effects of the liquid composition on the development of the vortical features of the flow, the vortical state reached after the second pairing, and the gas temperature and composition. They concluded that the mixing layer growth and main rotational characteristics are unaffected by liquid specificity; however, the global mixing is highly liquid specific. The analysis of the vorticity budgets showed that the small-scale vortical activity increases with increased fuel volatility.

Russo et al. (2014) studied the evaporation and condensation of water droplets in a turbulent channel flow in zero gravity at $Re_\tau = 150$ using DNS with the point particle approach and two-way coupling of mass, momentum, and heat between the two phases. The carrier fluid consisted of air and water vapor. One of the channel walls was heated while the other was cooled. This created a temperature gradient in the wall-normal direction and also a nonuniform mean vapor mass fraction. The objective of the study was to analyze the effects of phase change on the global heat transfer properties of the flow and on droplet motion and size distribution. The density of both the air and water vapor were time and space dependent, but their sum remained invariant to satisfy the zero divergence condition for the whole flow. The details of the pseudospectral numerical method are given by Kuerten (2006). The results show that initially the droplets migrate towards the channel walls due to turbophoresis (Reeks 1983), thus increasing the droplet concentration in the vicinity of the walls. Simultaneously, evaporation and condensation result in the droplets' growth near the cold wall and diminution near the warm wall. This also creates a gradient in water vapor concentration, directed from the cold to the warm wall. After reaching a steady state, the droplet concentration and mean droplet size become nearly constant. Turbulent diffusion of water vapor generates a mean flux of water vapor from the warm to the cold wall. Consequently, conservation of water mass results in a net mass flux of the droplets from the cold to the warm wall.

The results show that, at steady state, the heat transfer between the two walls for the droplet-laden flow, quantified by the Nusselt number, is 3.5 times larger than that of the single-phase flow and 2.6 times larger than that of a flow laden with solid spherical particles having the same diameter, response time ($\tau_p^+ = \tau_p u_\tau^2/\nu$), and specific heat as the droplets. This augmentation of heat transfer (by droplets versus solid particles) is due to the latent heat of vaporization, which reduces the droplet temperature near the hot wall, and the latent heat of condensation, which increases the droplet temperature near the cold wall. The results also show that, at steady state, the turbulence modulation of the carrier fluid by the droplets is the same as the modulation by solid particles. The Reynolds shear stresses and the TKE production are reduced in the wall region by the droplets. This finding is in contrast to that of Mashayek (1998), who found that droplets' evaporation enhanced the TKE production. In the simulation of Russo et al. (2014), both evaporation and condensation occur due to the presence of the hot and cold walls, resulting in a negligible net evaporation rate. The mean droplet diameter was found to be smaller near the warm wall than near the cold wall. Nucleation of droplets and droplet breakup were not accounted for in this study.

Kuerten & Vreman (2015) extended the DNS study of Russo et al. (2014) to include the effects of droplet collisions. The prescribed Weber number of the droplets was small enough that coalescence between colliding droplets was negligible. The droplets' overall volume fraction was in the range $0.55 \times 10^{-4} \leq \Phi_{vo} \leq 2.2 \times 10^{-4}$, and the corresponding number of droplets varied from 0.5×10^6 to 2×10^6. The results show that droplet collisions (i.e., four-way coupling) cause a significant reduction (about 76%) of the maximum local concentrations of the droplets near the channel walls, as compared to the two-way coupling case with the same overall Φ_{vo}. Regarding the dependence of droplet collisions on Φ_{vo}, Kuerten & Vreman (2015) stated that: "Elghobashi's diagram (Elghobashi 1994) indicates that the demarcation line between the two-way and four-way coupling regimes shifts toward lower volume fraction if the Stokes number becomes higher. However, in the present work, the Stokes number is only 10 in wall units, which shows that the effect of collisions on concentration in dilute flows is not limited to very high Stokes numbers" (p. 21).

Two comments related to the above statement are made here to clarify the diagram of Elghobashi (1994). First, the logarithmic-scale ordinate in the diagram is the Stokes number, $St = \tau_p/\tau_K$. The diagram shows that the demarcation line between the two-way and four-way regimes shifts toward lower volume fraction ($<10^{-3}$) for $\tau_p/\tau_K \geq 0.7$ since the maximum preferential accumulation of solid particles in isotropic turbulence occurs at $\tau_p/\tau_K = 1$ (Ferrante & Elghobashi 2003). In other words, particle collisions are expected to start before the local concentration reaches its peak. Second, if preferential accumulation occurs in a particle-laden turbulent flow, then the abscissa of the diagram should represent the local volume fraction, ϕ_v, instead of the overall volume fraction, Φ_{vo}, to determine whether the regime at a selected location is two-way or four-way coupling.

The heat transfer results of Kuerten & Vreman (2015) indicate that accounting for the droplet collisions (four-way coupling) reduces the Nusselt number by approximately 17% as compared to two-way coupling for the case with highest Φ_{vo}. This means that a reduction of 76% in the maximum ϕ_v near the wall resulted in only 17% reduction in Nusselt number. To explain this result, we should note here that the large increase in Nusselt number when inertial particles are present in the flow is caused totally by the direct convective heat transfer between the particles and the carrier fluid due to their temperature difference. The reason for this direct causality is that the two-way momentum coupling between the particles and fluid reduces the turbulent shear stresses, TKE, and hence the turbulent heat fluxes within the carrier fluid—for example, quantities proportional to $<u_i T_f>$, where u_i and T_f are the fluctuations of the local fluid velocity and temperature (see equations 20 and 21 in Kuerten & Vreman 2015).

The 76% reduction in the maximum ϕ_v near the hot wall reduces the total surface area of the droplets across which heat is transferred from the hot fluid. Consequently, the fluid temperature (as well as the temperature difference between the fluid and droplets) near the hot wall is higher for the colliding droplets than in the case of no collisions. Thus, the Nusselt number reduction for the four-way coupling case is not as severe as that of ϕ_v.

3.1.2. Deformable droplets of size $d < \eta$. Cristini et al. (2003) studied the deformation and breakup of sub-Kolmogorov droplets in stationary isotropic turbulence. The objective was to enhance the understanding of the droplet breakup process beyond the phenomenological models of Kolmogorov (1949) and Hinze (1955). At the scale of these droplets, the viscous stresses, $\mathcal{T}_\mu = \mu/\tau_K$, dominate the inertial stresses, $\mathcal{T}_\rho = \rho d^2/\tau_K^2$, since $\mathcal{T}_\mu/\mathcal{T}_\rho = \eta^2/d^2$. Consequently, the local velocity field in the vicinity of these droplets was assumed to be governed by the Stokes flow equations. Both the viscosity ratio of the droplet fluid to the carrier fluid and the corresponding density ratio were set equal to unity (neutrally buoyant droplets). The droplets were treated as

passive tracers with no effects on the carrier fluid. Under these conditions, it was assumed that the trajectory of a droplet center of mass is identical to that of the carrier fluid particle that coincided with it at an initial time. The velocity field of the stationary isotropic turbulence, at $Re_\lambda = 54$, was obtained using a pseudospectral DNS method.

The velocity field around a droplet was obtained by iteratively solving, at each time step, the boundary integral equation for the Stokes flow on a set of interfacial marker points that were distributed on the surface of the initially spherical droplet. That velocity field was matched with the velocity of the turbulent flow near the droplet location via linear expansion. The boundary conditions for the local Stokes flow velocity field around the deformable droplets were prescribed at the droplet interface by the continuous velocity and tangential stress and the discontinuous normal stress due to surface tension. The droplet interface was adaptively restructured, between time steps, to maintain uniform resolution of the pointwise curvature with a prescribed accuracy, as described in detail by Cristini et al. (2001). The results of Cristini et al. (2003) included the history of the deformation of two initially spherical droplets along their trajectories. Depending on the local shear/strain rates, the droplet deformation stages included stretched ellipsoids and dumbbells that led to neck thinning and pinch-off.

Biferale et al. (2014) studied the deformation and orientation statistics of sub-Kolmogorov ellipsoidal droplets in isotropic turbulence. Both the viscosity ratio of the droplet fluid to the carrier fluid and the corresponding density ratio were set equal to unity (neutrally buoyant droplets). The droplets were treated as passive tracers with no effects on the carrier fluid. Each of the simulated droplets followed the trajectory of the carrier fluid particle coinciding with its center at an initial time. The stationary homogeneous isotropic turbulent flow was computed via DNS at $Re_\lambda = 185$ and 400. The ellipsoidal droplet shape evolution was predicted via the phenomenological equation of Maffettone & Minale (1998) described earlier in Section 2.1.2. The prescribed initial droplet size was such that $d/\eta \leq 0.1$. The trajectories of 7×10^3 droplets for the $Re_\lambda = 185$ case and 15×10^3 droplets for the $Re_\lambda = 400$ case were computed. The results show, as expected, that increasing the capillary number, Ca, for a given τ_K increases the droplet deformation. The deformation of a typical droplet may follow a sequence of becoming oblate, becoming prolate, and then returning to a spherical shape. A critical capillary number was identified at which the droplet elongation along one or two directions becomes unbounded, which should eventually lead to droplet breakup.

Spandan et al. (2016) studied the deformation and orientation statistics of neutrally buoyant sub-Kolmogorov ellipsoidal droplets in turbulent TC flow. They followed the same approach of Biferale et al. (2014) and their own study of the sub-Kolmogorov bubbles (Spandan et al. 2017b) described above in Section 2.1.2. Spandan et al. (2016) used the term "zero-way coupling" as a name for the approach that considers the droplet as a massless passive tracer. However, "zero-way coupling" means no coupling, and certainly this is not the case of a tracer following the identical instantaneous Lagrangian motion of a fluid particle. "Tracer" or "passive scalar" are more appropriate names for this approach.

The droplet sizes were in the range $0.05 \leq d/\eta \leq 0.15$ even during the deformation. The DNS were performed for two inner cylinder Reynolds numbers ($Re_i = 2{,}500$ and 5,000), four capillary numbers ($Ca = 0.05$, 0.1, 0.2, and 0.3), and two viscosity ratios ($\hat{\mu} = 1$ and 100).

The statistical analysis of the droplet deformation was performed using the dimensionless deformation parameter D defined above in Section 2.1.2. The results show that the maximum values of D occur near both the rotating and stationary walls, and as expected, D increases with increasing the capillary number, Ca. However, the peak of the D profile moves away from the wall with increasing Ca. This is a result of the elastic collision model used for the interaction of

the droplet with the wall. The center of mass of a highly stretched droplet is displaced away from the wall as compared to that of a less-deformed droplet.

3.2. Droplets Larger than the Kolmogorov Length Scale ($d > \eta$)

In the following five subsections, we review studies on single-droplet deformation and evaporation in isotropic turbulence using LBM, single-droplet deformation in a turbulent channel flow using PFM, coalescence and breakup of large droplets in turbulent channel flow using PFM, dispersion of liquid droplets in isotropic turbulence using LBM-PFM, and the interaction between 3,130 fully resolved droplets and isotropic turbulence using VOF.

3.2.1. Single-droplet deformation and evaporation in isotropic turbulence using the lattice Boltzmann method. Albernaz et al. (2017) used a hybrid LBM to study the deformation and evaporation of a single droplet in stationary isotropic turbulence. In their hybrid method, the fluid density and velocity fields were obtained via LBM with a D3Q19 lattice and a multirelaxation time collision operator (d'Humières et al. 2002), but the internal energy conservation equation was solved by the finite difference scheme of Lallemand & Luo (2003). In the D3Q19 lattice, "D3" denotes 3D flow and "Q" refers to the first author of the paper by Qian et al. (1992). The number 19 indicates that a fluid point at the center of the cubic lattice interacts with the 18 neighboring points (12 points of intersection of the 3 midplanes with the edges of the cube, plus 6 points of intersection of the 3 midplanes at the 6 surfaces of the cube). A fluid point at the center of the cube has 18 possible velocity directions, plus a zero velocity. The internal energy equation contained a correction term proportional to the difference between the mean pressure of the domain and the initial reference pressure. The correction is needed for conditions close to the critical point where fluctuations of thermodynamic properties occur.

Forcing at low wave numbers using the method of Kareem et al. (2009) was applied at every time step to generate a statistically stationary velocity field for $73 \leq Re_\lambda \leq 133$. The pseudopotential method of Shan & Chen (1993) and Kupershtokh & Medvedev (2006) was used to simulate the droplet in the LBM. The liquid hexane droplet was surrounded by its vapor as the carrier fluid. The interface between the liquid and vapor was considered as a thin transition layer of finite width (several nodes of the lattice) where the density changes smoothly from one phase to the other. The ratio of the liquid density to that of the vapor was ~10. Additionally, the ratio of the liquid dynamic viscosity to that of the vapor was ~10, since both the liquid and the vapor had identical kinematic viscosity. The surface tension, σ, was calculated via the Young–Laplace equation, which relates the pressure jump across the interface to the product of σ and the local curvature (Landau & Lifshitz 1959). The initial temperature of both the liquid and the vapor was prescribed to be $0.9T_{\text{critical}}$ of hexane. The initial droplet diameter, d_o, ranged from 50η to 80η, which corresponds to the range from 2.4λ to 3.8λ.

The effect of surface tension on the droplet deformation was studied by varying the Ohnesorge number, $Oh = \mu_\ell/\sqrt{\rho_\ell \sigma\, d} = \sqrt{We_\ell}/Re_\ell$, in the range $4.2 \times 10^{-3} \leq Oh \leq 6 \times 10^{-3}$, where μ_ℓ and ρ_ℓ are the dynamic viscosity and density of the droplet.

Some interesting results of this study are: (*a*) For a fixed Re_λ, increasing d_o increases the kinetic energy of the carrier fluid and reduces the kinetic energy of the droplet since the total kinetic energy is a function of the fixed Re_λ. (*b*) The droplet deformation increases with increasing d_o due to the increase of Weber number. (*c*) Reducing the surface tension increases the fluctuations of the thermodynamic properties, thus increasing the evaporation rate. (*d*) At the droplet surface, low-temperature regions are associated with stronger curvature, whereas higher temperature occurs in flatter surface regions (**Figure 4**). (*e*) Droplet volume fluctuations are correlated with vapor

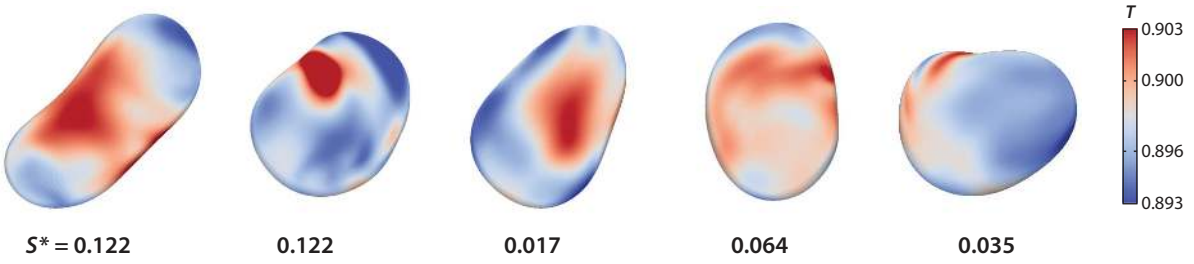

Figure 4

Temperature distribution over the droplet surface for different values of the deformation parameter, $S^* = (S - S_0)/S_0$, where S is the instantaneous area of the droplet surface and S_0 is the equivalent surface area of a sphere whose volume is identical to that of the deformed droplet. Figure adapted from Albernaz et al. (2017) with permission from Cambridge University Press.

temperature fluctuations. Strong correlations occur between positive temperature fluctuations and vapor condensation.

3.2.2. Single-droplet deformation in a turbulent channel flow using the phase field model. Scarbolo & Soldati (2013) used the PFM (see Section 1) of Gurtin et al. (1996) to study the deformation of a single droplet released in a fully developed turbulent channel flow at $Re_\tau = 100$. The ratios of the liquid density and viscosity of the droplet to those of the carrier fluid were prescribed to be equal to unity. As described earlier in Section 1, the forcing term representing the surface tension effects was added to the Navier–Stokes equations. The modified Navier–Stokes equations were solved together with the phase field transport equation of Cahn & Hilliard (1959). The initial droplet diameter was $d_o = 0.8H$, where H is half the channel height, and d_o/η ranged from 7.7 to 16.7. The Weber number, $We = (\rho u_\tau^2 H)/\sigma$, was in the range $5.3 \times 10^{-3} \leq We \leq 42.4 \times 10^{-3}$. For that range of We, the mass loss at the end of the simulation varied from 4% to 14%. The results show that the TKE reaches its minimum value at the interface. The vorticity peak occurs at a distance of $\sim d/4$ from the droplet interface, and the magnitude of that peak decreases with decreasing We (see Scarbolo & Soldati 2013, figure 5).

Scarbolo et al. (2013) compared the performance of PFM with that of LBM (described in Section 3.2.1 above) in simulating the deformation of a single 2D cylindrical droplet in simple shear flows. The comparison showed that the PFM's computational cost is almost three times higher than that of LBM. However, the results of the PFM appear to be more accurate, in that the spurious currents of the local kinetic energy created along the droplet interface were smaller in PFM than in LBM by two orders of magnitude (see Scarbolo et al. 2013, figure 1).

3.2.3. Coalescence and breakup of large droplets in turbulent channel flow using the phase field model. Scarbolo et al. (2015) used the above-described PFM in simulating droplets with initial number $N_0 = 256$ and volume fraction $\Phi_v = 0.054$ in a DNS of a fully developed turbulent channel flow at $Re_\tau = 150$. The objective was to study the interactions between the droplets. The ratios of the liquid density and viscosity of the droplet to those of the carrier fluid were prescribed to be equal to unity. The initial droplet diameter was $d_o = 0.4H$, where H is half the channel height, and d_o/η ranged from 15.9 to 37. The interface thickness, ξ, was a constant prescribed via the Cahn number, $Cb = \xi/H = 0.0185$, which resulted in η/ξ ranging from 0.36 to 0.84, thus minimizing the smallest eddies' effects on distorting the interface. The mass loss at the end of the simulation varied from 2% to 10% for the range of $0.18 \leq We \leq 2.8$. The results show that under the selected conditions and fluid properties, droplets migrate away from the wall toward

the channel center. The study identified two regimes of droplet interactions based on the Weber number. For $We < 1$, the relatively large surface tension prevents droplet breakup and allows coalescence events to prevail. Eventually, for $t^+ > 2{,}000$ (in wall units), the number of the merged droplets becomes $<N_0$ and their separation distances increase, resulting in diminished collisions.

In contrast, for $We > 1$, the droplet breakup and coalescence processes occur simultaneously during an early transition period. This is followed at large t^+ by a dynamic equilibrium state, at which the number of droplets reaches an asymptotic value that is about an order of magnitude larger than that for the case of $We < 1$.

Scarbolo et al. (2016) performed DNS with the same flow conditions and fluid properties as Scarbolo et al. (2015) to investigate turbulence modification by dispersed deformable droplets. The results show that, for $We > 1$, the normalized wall shear stress or friction coefficient, C_f, for the channel flow is not affected by the deformed droplets and that its temporal development is nearly the same as that of the single-phase flow. However, for $We < 1$, the temporal development of C_f shows a gradual increase at early times, reaching a peak at $1{,}000 \leq t^+ \leq 2{,}000$, followed by a gradual reduction. The physical explanation for these observations was not provided.

Roccon et al. (2017) extended the DNS study of Scarbolo et al. (2016) by relaxing the restriction of a unity viscosity ratio to examine the effects of varying the viscosity of the droplet. Five different values of the dynamic viscosity ratio ($\hat{\mu} = 0.01$, 0.1, 1, 10, and 100) and three values of Weber number ($We = 0.75$, 1.5, and 3) were studied, providing a total of 15 test cases. The initial number of droplets was $N_0 = 256$, with volume fraction $\Phi_{vo} = 0.183$ and initial droplet diameter $0.6H$. The results show that, for all test cases, the deformable droplets migrate away from the wall and reduce the wall friction slightly, as indicated by a ~2–4% increase of the average mean velocity in the central zone of the channel.

Qualitatively, the results show that, as expected, increasing the droplet viscosity or surface tension decreases the breakup rate. For the case of the highest surface tension, $We = 0.75$, the droplets' coalescence rate overtakes their breakup rate for all values of $\hat{\mu}$, resulting in a gradual reduction of the number of droplets (**Figure 5**), which reaches an asymptotic value of $\sim 0.04N_0$

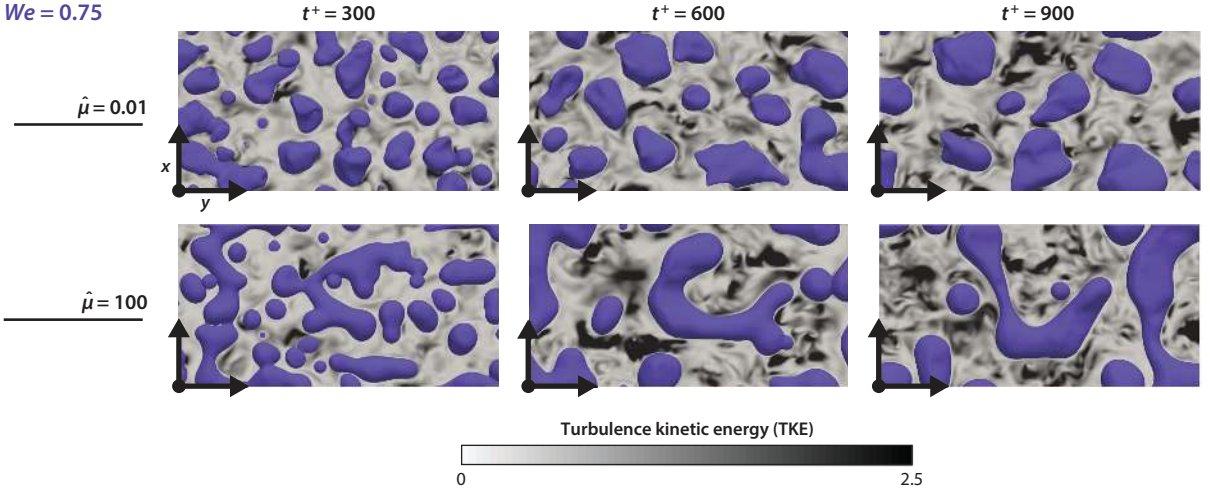

Figure 5

Temporal evolution of droplets for $We = 0.75$ and for two viscosity ratios, $\hat{\mu} = 0.01$ (*top row*) and $\hat{\mu} = 100$ (*bottom row*). Each panel refers to a given time instant ($t^+ = 300$, 600, or 900). Isocontours of turbulence kinetic energy computed on a plane passing through the channel center are shown in gray scale. Figure adapted from Roccon et al. (2017) with permission from the American Physical Society.

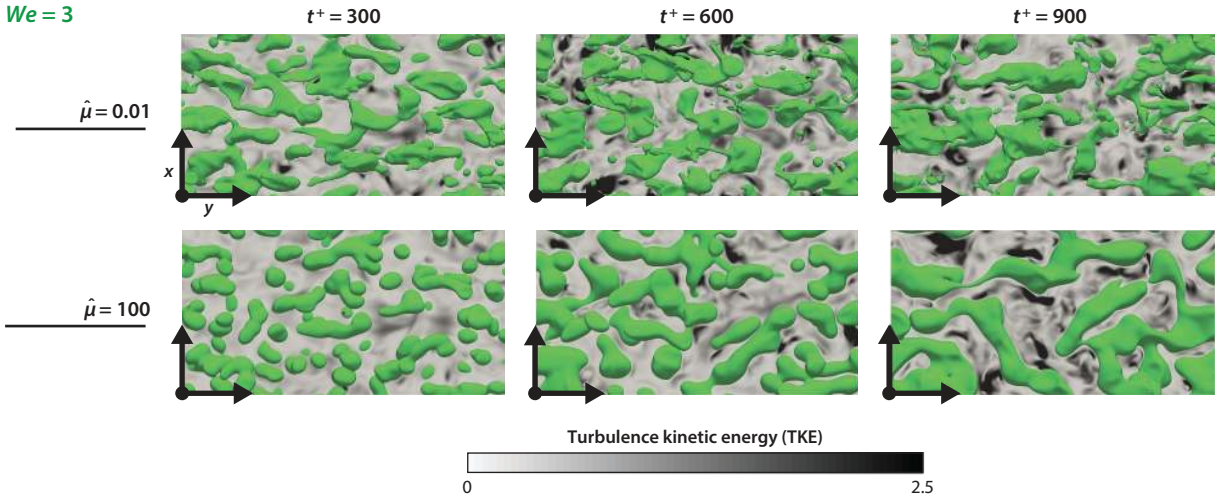

Figure 6

Temporal evolution of droplets for $We = 3$ and for two viscosity ratios, $\hat{\mu} = 0.01$ (*top row*) and $\hat{\mu} = 100$ (*bottom row*). Each panel refers to a given time instant ($t^+ = 300$, 600, or 900). Isocontours of turbulence kinetic energy computed on a plane passing through the channel center are shown in gray scale. Figure adapted Roccon et al. (2017) with permission from the American Physical Society.

after $t^+ = 1{,}000$. For the lowest surface tension, $We = 3$, the effect of varying $\hat{\mu}$ becomes more pronounced (**Figure 6**). For $\hat{\mu} \leq 1$, the breakup rate increases, and the asymptotic number of droplets is $\sim 0.4N_0$. For $\hat{\mu} = 10$, the breakup rate decreases, and the number of droplets reaches $0.1N_0$. For $\hat{\mu} = 100$, the coalescence rate prevails, and the number of droplets diminishes to $0.01N_0$.

These results show that lowering the droplet viscosity (relative to that of the carrier fluid), at a fixed surface tension, enhances the droplet deformation and the eventual breakup. The results also show that, as expected, the mean curvature of the interface between the droplet and the carrier fluid depends on $\hat{\mu}$. The interface is defined as the isosurface of the scalar phase field function, $\phi(\mathbf{x}, t) = 0$, and its mean curvature is $\kappa = \nabla \cdot (-\nabla\phi/|\nabla\phi|)$ (Sun & Beckermann 2007). The case of lowest surface tension, $We = 3$, and smallest viscosity ratio, $\hat{\mu} = 0.01$, resulted in strong curvature and breakup, leading to the creation of small droplets (**Figure 6**). In contrast, for the same surface tension and a viscosity ratio of $\hat{\mu} = 100$, large elongated droplets with relatively small curvatures were created (**Figure 6**).

3.2.4. Dispersion of liquid droplets in isotropic turbulence using the lattice Boltzmann method and phase field model. Komrakova et al. (2015) used the free-energy LBM of Swift et al. (1996), in which the diffuse interface evolves naturally according to thermodynamics. This free-energy LBM is a hybrid of LBM and PFM. As described earlier in Section 1, two probability density functions, $f_i^n(\mathbf{x}, t)$ for $n = 2$, were used: one to solve the continuity and Navier–Stokes equations for the carrier fluid and another to solve the Cahn–Hilliard equation (Cahn & Hilliard 1959). A single relaxation time collision operator (Bhatnagar et al. 1954) was used in the solution.

The D3Q19 lattice (Section 3.2.1) was used to perform DNS of stationary isotropic turbulence generated by the linear forcing method of Lundgren (2003). The periodic cubic computational domain contained a maximum of $1{,}000^3$ dimensionless lattice units (lu), where the Kolmogorov length scale η is ~1–10 lu. The Reynolds number, Re_λ, could not be prescribed as an input

parameter since the velocity, u_{rms}, is not known a priori. Only three parameters were used to prescribe the turbulent two-phase flow: the droplets volume fraction, Φ_{vo}, the viscosity ratio, $\hat{\mu}$, and the capillary number, $Ca = \tau/\tau_K = (\eta\,\mu_f)/(\sigma\,\tau_K)$, where μ_f is the dynamic viscosity of the carrier fluid. The density ratio of the droplet to that of the carrier fluid was set to unity, and the viscosity ratio was $0.3 \leq \hat{\mu} \leq 1$. The DNS starts at $t = 0$ with a single droplet placed in the computational domain with a volume fraction range $0.001 \leq \Phi_{vo} \leq 0.2$. The initial droplet diameter was in the range of 20–30η. The droplet breaks up due to the turbulent stresses in the carrier fluid, as shown in **Figure 7**. The Reynolds number was computed from the DNS

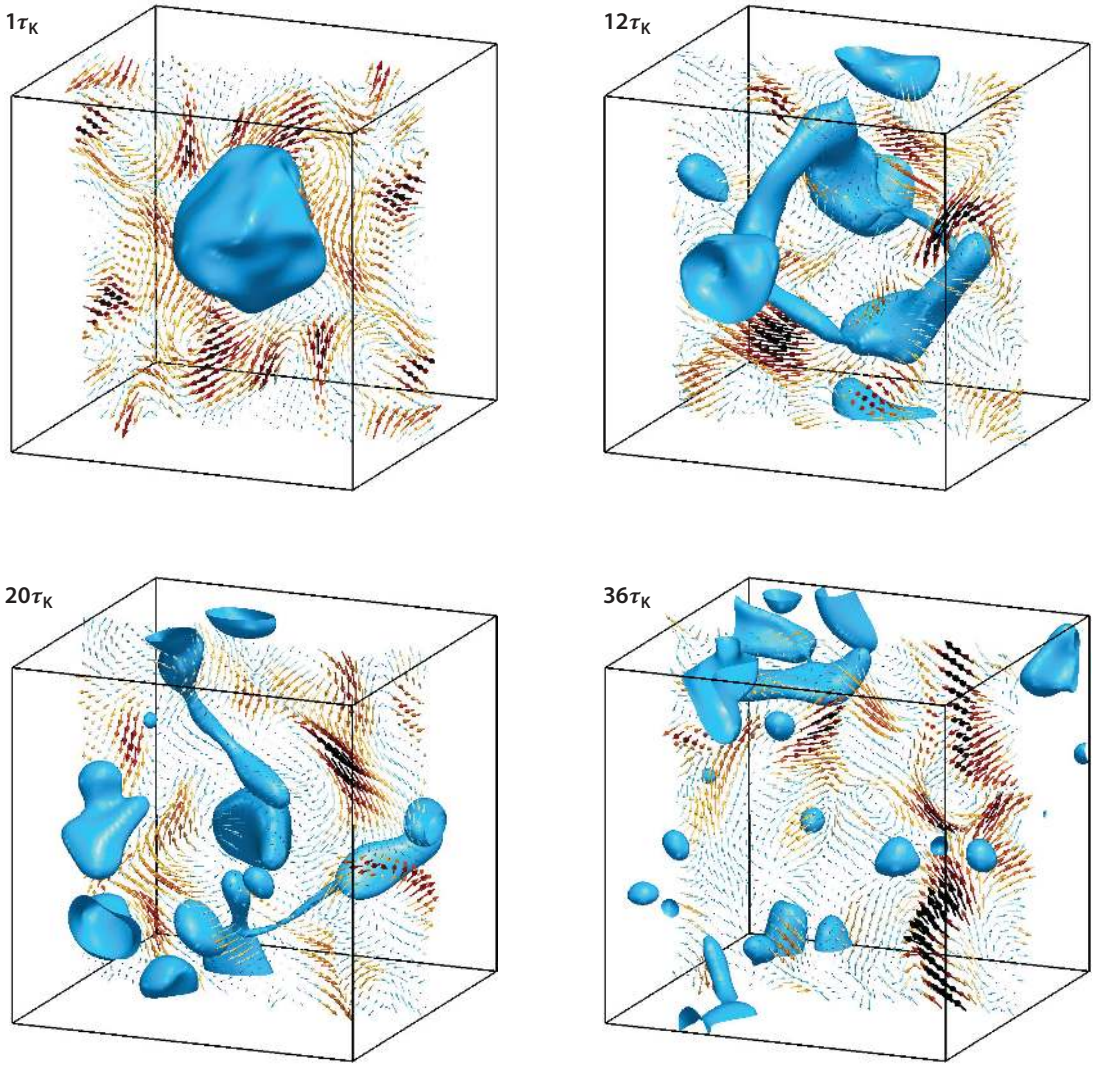

Figure 7

Isosurfaces of the scalar phase field $\phi = 0$ representing the surface of the dispersed liquid droplet and velocity vectors at different time instants relative to the Kolmogorov timescale, τ_K, for the case with $\eta = 1$ (lattice units), viscosity ratio $\hat{\mu} = 1$, density ratio $= 1$, and capillary number $Ca = 0.1$. The dispersed phase volume fraction is $\Phi_v = 0.03$. The initial single droplet is placed in the isotropic turbulence at $t = 0$. Figure adapted from Komrakova et al. (2015) with permission from *AIChE Journal*.

results for the case shown in **Figure 7** as $Re_\lambda = 42$ (A.E. Komrakova, personal communication). The study points out the following limitations of the DNS using LBM-PFM: (*a*) Coalescence occurs when the interfaces of multiple droplets occupy the same computational cell. Thus, in order to suppress unphysical coalescence, it is necessary to resolve the liquid film between the droplets, which requires prohibitive mesh refinement (Shardt et al. 2013). (*b*) Dissolution of small droplets is an inherent property of the numerical method (Keestra et al. 2003). The dissolution rate increases as the droplet size decreases. To minimize the dissolution, one needs to increase the resolution by keeping the droplet diameter in the range of $20–30\eta$. (*c*) It is not possible to obtain an accurate TKE spectrum of a two-phase turbulent flow. It is known that LBM is prone to generate spurious currents due to discretization of the velocity space. The order of magnitude of the spurious currents can be the same as that of the actual velocity field. In addition, the spurious currents appear within the diffuse interface and interact with the small-scale motion, leading to a significant unphysical energy gain at high wave numbers.

3.2.5. The interaction between 3,130 fully resolved droplets and isotropic turbulence using volume of fluid. Dodd & Ferrante (2016) performed DNS of decaying isotropic turbulence, at an initial $Re_\lambda = 83$, laden with 3,130 nonvaporizing droplets of size $d \approx 20\eta \approx \lambda$. The ranges of the density and dynamic viscosity ratios were $1 \leq \hat{\rho} \leq 100$ and $1 \leq \hat{\mu} \leq 100$, respectively. The Weber number based on the root mean squared velocity of the carrier fluid was in the range $0.1 \leq We_{\text{rms}} \leq 5$. The volume fraction of the droplets was $\Phi_v = 0.05$, and the mass fraction ranged from 0.5 to 5.

Before discussing the results of the simulations, it is worth describing the novel method developed by Dodd & Ferrante (2016) for solving the Poisson equation for the pressure in incompressible immiscible two-fluid flows with large density and dynamic viscosity ratios. The method is described in detail by Dodd & Ferrante (2014). It is well known that the numerical solution of the Navier–Stokes equations of two-fluid flows with nonuniform density requires solving a variable-coefficient Poisson equation for the pressure of the form

$$\nabla \cdot \left(\frac{1}{\rho^{n+1}} \nabla p^{n+1} \right) = \frac{1}{\Delta t} \nabla \cdot \mathbf{u}^*, \qquad 10.$$

where $\mathbf{u}^*$ is the approximate fluid velocity at time step $n+1$. Solving Equation 10 is conventionally performed using iterative multigrid methods (Gueyffier et al. 1999) or multigrid-preconditioned Krylov methods (Sussman & Puckett 2000). All these methods are much slower than the fast Poisson solvers (e.g., fast Fourier transform). However, these require the coefficient of ∇p^{n+1} to be a constant, whereas the coefficient $\frac{1}{\rho^{n+1}}$ on the left-hand side of Equation 10 varies in space and time. To overcome this problem, Dong & Shen (2012) split the product inside the parenthesis in Equation 10 in such a way as to render the variable coefficient of ∇p^{n+1} a constant. The first step is to approximate the product on the left-hand side of Equation 10 as

$$\frac{1}{\rho^{n+1}} \nabla p^{n+1} \approx \frac{1}{\rho_0} \nabla p^{n+1} + \left(\frac{1}{\rho^{n+1}} - \frac{1}{\rho_0} \right) \nabla p^*, \qquad 11.$$

where $\rho_0 = \min(\rho_1, \rho_2)$ and $p^* = 2p^n - p^{n-1}$. Then, substitution of Equation 11 into Equation 10 results in

$$\nabla^2 p^{n+1} = \nabla \cdot \left[\left(1 - \frac{\rho_0}{\rho^{n+1}} \right) \nabla p^* \right] + \frac{\rho_0}{\Delta t} \nabla \cdot \mathbf{u}^*, \qquad 12.$$

which can be solved using fast Poisson solvers. Dodd & Ferrante (2014) compared the accuracy and speed of solving Equations 10 and 12 for several canonical two-phase flows at density and

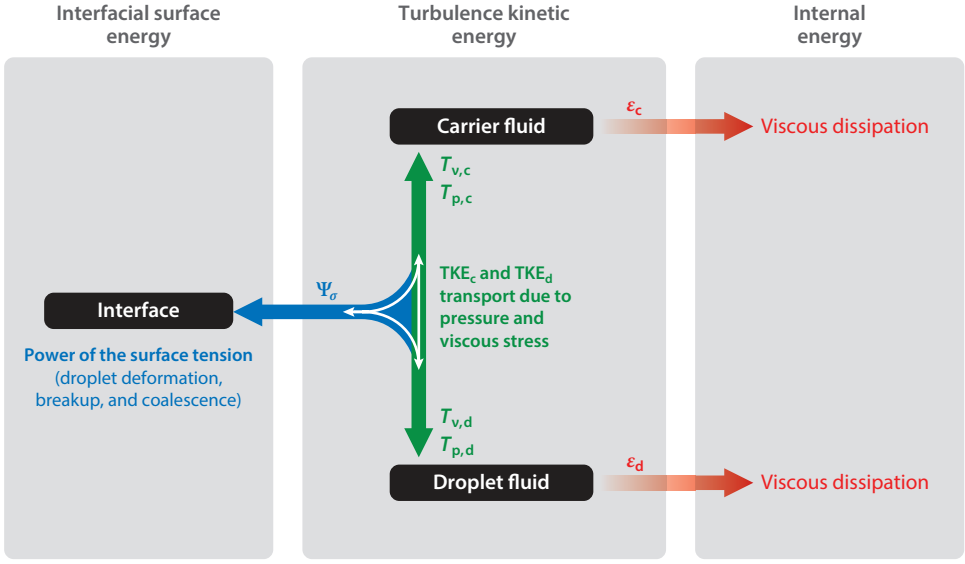

Figure 8

Schematic showing turbulence kinetic energy (TKE) exchanges between the droplets and carrier fluid turbulence. The three bounding rectangles from left to right represent the interactions between interfacial surface energy, TKE, and internal energy. The blue arrow represents the two-way exchange between TKE and interfacial surface energy by the power of the surface tension, Ψ_σ. The green arrows denote the transport of TKE between the two fluids while exchanging TKE for surface energy via Ψ_σ. The subscripts c and d in the figure denote the carrier fluid and droplets, respectively. The red arrows represent the transformation of TKE of the carrier fluid and droplet into internal energy by viscous dissipation. Figure adapted from Dodd & Ferrante (2016) with permission from Cambridge University Press.

dynamic viscosity ratios up to 10^4. They concluded that the new split method is at least an order of magnitude faster than that of Equation 10 for the same accuracy level.

To explain the TKE exchanges between the droplets and the carrier fluid, Dodd & Ferrante (2016) derived three TKE transport equations for the droplet phase, the carrier fluid, and the combined two-fluid flow (see Dodd & Ferrante 2016, equations B19, B20, B21, and C8). For the first two equations, the TKE decay rate is governed by the sum of the viscous dissipation rate, $-\varepsilon$, the viscous power, T_v, and pressure power, T_p. For the combined two-fluid flow, the TKE decay rate equals the sum of the viscous dissipation rate and the power due to surface tension, Ψ_σ, which is the rate of work done by the surface tension forces on the fluid. Surface tension Ψ_σ can be a source or sink of TKE, depending on whether the total surface area of droplets decreases (e.g., coalescence) or increases (e.g., breakup), respectively. **Figure 8** shows a schematic of the TKE exchanges according to the three TKE transport equations.

Dodd & Ferrante performed DNS for seven cases, A through G, by varying We_{rms}; the density ratio, $\hat{\rho}$; or the dynamic viscosity ratio, $\hat{\mu}$. Increasing We_{rms} from 0.1 in case B to 5 in case D showed that at the end of the simulation the number of droplets decreased due to coalescence relative to their initial number by about 20% in case B and increased due to breakup by about 27% in case D. In case B, the power Ψ_σ due to coalescence represents a source of TKE equal to about 50% of the magnitude of the viscous dissipation rate.

Figure 9 compares the viscous dissipation rate for cases E and F, where both have the same dynamic viscosity ratio, $\hat{\mu} = 10$, but their density ratios $\hat{\rho}$ were 1 and 100, respectively. The

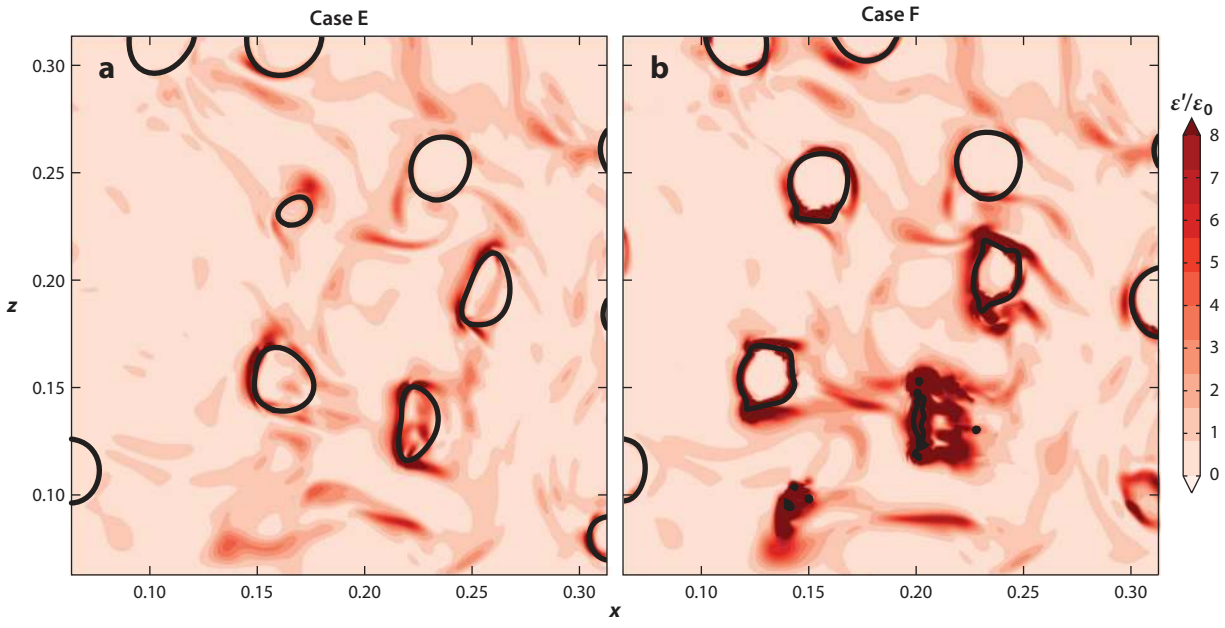

Figure 9

Comparison of the viscous dissipation rate in Dodd & Ferrante's (2016) case E (*a*) and case F (*b*). Both cases have the same dynamic viscosity ratio, $\hat{\mu} = 10$, but case E has a density ratio of $\hat{\rho} = 1$, whereas we have $\hat{\rho} = 100$ in case F. Figure adapted from Dodd & Ferrante (2016) with permission from Cambridge University Press.

response time, τ_d, of the denser droplets in case F is 100 times that of the droplets in case E. Thus the F droplets generate higher fluid strain rates near their surfaces than do the E droplets, and hence the dissipation rates are higher in F, as shown in **Figure 9**.

SUMMARY POINTS

1. Significant progress has been made during the past 20 years in direct numerical simulation (DNS) of turbulent flows laden with droplets or bubbles. This progress is due to continuing development of the numerical methods discussed above and advances in supercomputer hardware and software.
2. The phenomenological equation of Maffettone & Minale (1998) provides a powerful tool for accounting for shape changes of deformable bubbles or droplets smaller than the Kolmogorov length scale, η.
3. All the reviewed DNS studies of fully resolved droplets or bubbles, except that of Dodd & Ferrante (2016), restricted the density and viscosity ratios of the two interacting phases between 1 and 10. Both the density and viscosity ratios were equal to 10^2 in Dodd & Ferrante's (2016) study. Furthermore, Dodd & Ferrante (2014) validated their numerical method with Prosperetti's (1981) analytical solution of the capillary wave for density and viscosity ratios up to 10^4 and with the experimental data of Beard (1976) for a falling droplet with a density ratio of 10^3.

4. The phase field model (PFM) provides qualitatively interesting results; however, it suffers from the following drawbacks: (*a*) The large width of the interface region (4–8 cells) leads to errors in the curvature (Jacqmin 1999). (*b*) Mass conservation is not satisfied (Yue et al. 2007), as confirmed by Scarbolo & Soldati (2013) and Scarbolo et al. (2015), who showed in their studies that the mass loss at the end of the simulation varied from 4% to 14% and from 2% to 10%, respectively. This inability to conserve mass renders the PFM quite inaccurate for cases involving vaporization or condensation, as well as droplet motion, in highly vortical flows.

FUTURE ISSUES

1. Due to the complexity of turbulent flows laden with droplets or bubbles, the experimental data needed to validate the DNS results are virtually nonexistent. The needed experimental data should provide local instantaneous measurements of the velocity fields of both the carrier fluid and the dispersed phase in addition to instantaneous images of shape changes of the latter.
2. Since large-eddy simulation will be used for the foreseeable future to predict turbulent multiphase flows at practical Reynolds numbers, accurate subgrid scale (SGS) models need to be developed and validated by DNS results, such as those described above. Accurate SGS models do not presently exist.

DISCLOSURE STATEMENT

The author is not aware of any biases that might be perceived as affecting the objectivity of this review.

ACKNOWLEDGMENTS

The author thanks Professors William Sirignano, Andrea Prosperetti, Detlef Lohse, Alfredo Soldati, and Antonino Ferrante for their helpful comments on the first draft of this article.

LITERATURE CITED

Albernaz DL, Do-Quang M, Hermanson JC, Amberg G. 2017. Droplet deformation and heat transfer in isotropic turbulence. *J. Fluid Mech.* 820:61–85

Anderson DM, McFadden GB, Wheeler AA. 1998. Diffuse-interface methods in fluid mechanics. *Annu. Rev. Fluid Mech.* 30:139–65

Auton T. 1987. The lift force on a spherical body in a rotational flow. *J. Fluid Mech.* 183:199–218

Auton T, Hunt J, Prud'homme M. 1988. The force exerted on a body in inviscid unsteady non-uniform rotational flow. *J. Fluid Mech.* 197:241–57

Balachandar S, Eaton J. 2010. Turbulent dispersed multiphase flow. *Annu. Rev. Fluid Mech.* 42:111–33

Beard K. 1976. Terminal velocity and shape of cloud and precipitation drops aloft. *J. Atmos. Sci.* 33:851–64

Bhatnagar PL, Gross EP, Krook M. 1954. A model for collision processes in gases. I. Small amplitude processes in charged and neutral one-component systems. *Phys. Rev.* 94:511–25

Biferale L, Meneveau C, Verzicco R. 2014. Deformation statistics of sub-Kolmogorov-scale ellipsoidal neutrally buoyant drops in isotropic turbulence. *J. Fluid Mech.* 754:184–207

Cahn JW, Hilliard JE. 1959. Free energy of a nonuniform system. III. Nucleation in a two-component incompressible fluid. *J. Chem. Phys.* 31:688–99
Carl M, Behrendt T, Fleing C, Frodermann M, Heinze J, et al. 2001. Experimental and numerical investigation of a planar combustor sector at realistic operating conditions. *J. Eng. Gas Turbines Power* 123:811–16
Chen M, Kontomaris K, McLaughlin J. 1998. Direct numerical simulation of droplet collisions in a turbulent channel flow. Part II: collision rates. *Int. J. Multiph. Flow* 24:1105–38
Clift R, Grace J, Weber ME. 1978. *Bubbles, Drops, and Particles*. Mineola, NY: Dover
Cristini V, Blawzdziewicz J, Loewenberg M. 2001. An adaptive mesh algorithm for evolving surfaces: simulations of drop breakup and coalescence. *J. Comput. Phys.* 168:445–63
Cristini V, Blawzdziewicz J, Loewenberg M, Collins L. 2003. Breakup in stochastic stokes flows: sub-Kolmogorov drops in isotropic turbulence. *J. Fluid Mech.* 492:231–50
de Tullio M, Pascazio G. 2016. A moving-least-squares immersed boundary method for simulating the fluid–structure interaction of elastic bodies with arbitrary thickness. *J. Comput. Phys.* 325:201–25
Desjardins O, Moureau V, Pitsch H. 2008. An accurate conservative level set/ghost fluid method for simulating turbulent atomization. *J. Comput. Phys.* 227:8395–416
d'Humières D, Ginzburg I, Krafczyk M, Lallemand P, Luo L. 2002. Lattice Boltzmann multiple-relaxation-time models in three dimensions. *Proc. R. Soc. A* 360:427–51
Dodd M, Ferrante A. 2014. A fast pressure-correction method for incompressible two-fluid flows. *J. Comput. Phys.* 273:416–34
Dodd M, Ferrante A. 2016. On the interaction of Taylor length scale size droplets and isotropic turbulence. *J. Fluid Mech.* 806:356–412
Dong S, Shen J. 2012. A time-stepping scheme involving constant coefficient matrices for phase-field simulations of two-phase incompressible flows with large density ratios. *J. Comput. Phys.* 231:5788–804
Druzhinin O, Elghobashi S. 1998. Direct numerical simulations of bubble-laden turbulent flows using the two-fluid formulation. *Phys. Fluids* 10:685–97
Druzhinin O, Elghobashi S. 2001. Direct numerical simulation of a spatially-developing three-dimensional bubble-laden mixing layer with two-way coupling. *J. Fluid Mech.* 429:23–61
Elghobashi S. 1994. On predicting particle-laden turbulent flows. *Appl. Sci. Res.* 52:309–29
Elghobashi S, Prosperetti A. 2009. Preface. *Int. J. Multiph. Flow* 35:791
Elghobashi S, Truesdell G. 1993. On the two-way interaction between homogeneous turbulence and dispersed solid particles. I: turbulence modification. *Phys. Fluids* 5:1790–801
Ferrante A, Elghobashi S. 2003. On the physical mechanisms of two-way coupling in particle-laden isotropic turbulence. *Phys. Fluids* 15:315–29
Ferrante A, Elghobashi S. 2004. On the physical mechanisms of drag reduction in a spatially-developing turbulent boundary layer laden with microbubbles. *J. Fluid Mech.* 503:345–55
Ferrante A, Elghobashi S. 2007. On the effects of microbubbles on the Taylor–Green vortex flow. *J. Fluid Mech.* 572:145–77
Gueyffier D, Li J, Nadim A, Scardovelli R, Zaleski S. 1999. Volume-of-fluid interface tracking with smoothed surface stress methods for three-dimensional flows. *J. Comput. Phys.* 152:423–56
Guido S, Minale M, Maffettone P. 2000. Drop shape dynamics under shear-flow reversal. *J. Rheol.* 44:1385–99
Gurtin ME, Fried E, Anand L. 2010. *The Mechanics and Thermodynamics of Continua*. Cambridge, UK: Cambridge Univ. Press
Gurtin ME, Polignone D, Vinals J. 1996. Two-phase binary fluids and immiscible fluids described by an order parameter. *Math. Models Methods Appl. Sci.* 6:815–31
Hinze J. 1955. Fundamentals of the hydrodynamic mechanism of splitting in dispersion processes. *AIChE J.* 1:289–95
Jacqmin D. 1999. Calculation of two-phase Navier–Stokes flows using phase-field modeling. *J. Comput. Phys.* 155:96–127
Kareem WA, Izawa S, Xiong AK, Fukunishi Y. 2009. Lattice Boltzmann simulations of homogeneous isotropic turbulence. *Comput. Math. Appl.* 58:1055–61
Keestra B, Van Puyvelde P, Anderson P, Meijer HEH. 2003. Diffuse interface modeling of the morphology and rheology of immiscible polymer blends. *Phys. Fluids* 15:2567–75

Kolmogorov A. 1949. On the disintegration of drops in turbulent flow. *Dokl. Akad. Nauk* 66:825–28
Komrakova AE, Eskin D, Derksen JJ. 2015. Numerical study of turbulent liquid-liquid dispersions. *AIChE J.* 61:2618–33
Kuerten J. 2006. Subgrid modeling in particle-laden channel flow. *Phys. Fluids* 18:025108
Kuerten J, Vreman A. 2015. Effect of droplet interaction on droplet-laden turbulent channel flow. *Phys. Fluids* 27:053304
Kupershtokh A, Medvedev D. 2006. Lattice Boltzmann equation method in electrohydrodynamic problems. *J. Electrost.* 64:581–85
Lallemand P, Luo LS. 2003. Hybrid finite-difference thermal lattice Boltzmann equation. *Int. J. Mod. Phys.* 17:41–47
Landau L, Lifshitz E. 1959. *Fluid Mechanics*. Oxford: Pergamon
Leclercq P, Bellan J. 2005. Direct numerical simulation of gaseous mixing layers laden with multicomponent-liquid drops: liquid-specific effects. *J. Fluid Mech.* 533:57–94
Lu J, Biswas S, Tryggvason G. 2006. A DNS study of laminar bubbly flows in a vertical channel. *Int. J. Multiph. Flow* 32:643–60
Lu J, Fernandez A, Tryggvason G. 2005. The effect of bubbles on the wall drag in a turbulent channel flow. *Phys. Fluids* 17:095102
Lu J, Tryggvason G. 2006. Numerical study of turbulent bubbly downflows in a vertical channel. *Phys. Fluids* 18:103302
Lu J, Tryggvason G. 2008. Effect of bubble deformability in turbulent bubbly upflow in a vertical channel. *Phys. Fluids* 20:040701
Lu J, Tryggvason G. 2013. Dynamics of nearly spherical bubbles in a turbulent channel upflow. *J. Fluid Mech.* 732:166–89
Lundgren T. 2003. Linearly forced isotropic turbulence. In *Annual Research Briefs 2003*, pp. 461–73. Stanford, CA: Cent. Turbul. Res.
Madavan N, Deutsch S, Merkle C. 1984. Reduction of turbulent skin friction by microbubbles. *Phys. Fluids* 27:356–63
Maffettone P, Minale M. 1998. Equation of change for ellipsoidal drops in viscous flow. *J. Non-Newton. Fluid Mech.* 78:227–41
Mashayek F. 1998. Droplet-turbulence interactions in low-Mach-number homogeneous shear two-phase flows. *J. Fluid Mech.* 367:163–203
Maxey MR. 2017. Simulation methods for particulate flows and concentrated suspensions. *Annu. Rev. Fluid Mech.* 49:171–93
Maxey MR, Riley J. 1983. Equation of motion for a small rigid sphere in a nonuniform flow. *Phys. Fluids* 26:883–89
Mazzitelli I, Lohse D, Toschi F. 2003. On the relevance of the lift force in bubbly turbulence. *J. Fluid Mech.* 488:283–313
Miller R, Bellan J. 1999. Direct numerical simulation of a confined three-dimensional gas mixing layer with one evaporating hydrocarbon-droplet-laden stream. *J. Fluid Mech.* 384:293–338
Njobuenwu DO, Fairweather M. 2015. Dynamics of single, non-spherical ellipsoidal particles in a turbulent channel flow. *Chem. Eng. Sci.* 123:265–82
Osher S, Fedkiw R. 2001. Level set methods: an overview and some recent results. *J. Comput. Phys.* 169:463–502
Prosperetti A. 1981. Motion of two superposed viscous fluids. *Phys. Fluids* 24:1217–23
Prosperetti A. 2017. Vapor bubbles. *Annu. Rev. Fluid Mech.* 49:221–48
Qian D, McLaughlin J, Sankaranarayanan K, Sundaresan S, Kontomaris K. 2006. Simulation of bubble breakup dynamics in homogeneous turbulence. *Chem. Eng. Comm.* 193:1038–63
Qian YH, d'Humières D, Lallemand P. 1992. Lattice BGK models for Navier-Stokes equation. *Europhys. Lett.* 17:479–84
Reeks MW. 1983. The transport of discrete particles in inhomogeneous turbulence. *J. Aerosol Sci.* 14:729–39
Risso F, Fabre J. 1998. Oscillations and breakup of a bubble immersed in a turbulent field. *J. Fluid Mech.* 806:323–55
Roccon A, Paoli MD, Zonta F, Soldati A. 2017. Viscosity-modulated breakup and coalescence of large drops in bounded turbulence. *Phys. Rev. Fluids* 2:083603

Russo E, Kuerten JGM, van der Geld CWM, Geurts BJ. 2014. Water droplet condensation and evaporation in turbulent channel flow. *J. Fluid Mech.* 749:666–700
Saffman PG. 1965. The lift on a small sphere in a slow shear flow. *J. Fluid Mech.* 22:385–400
Saffman PG, Turner J. 1956. On the collision of drops in turbulent clouds. *J. Fluid Mech.* 1:16–30
Sankaranarayanan K, Kevrekidis I, Sundaresan S, Lu J, Tryggvason G. 2003. A comparative study of lattice Boltzmann and front-tracking finite-difference methods for bubble simulations. *Int. J. Multiph. Flow* 29:109–16
Scarbolo L, Bianco F, Soldati A. 2015. Coalescence and breakup of large droplets in turbulent channel flow. *Phys. Fluids* 27:073302
Scarbolo L, Bianco F, Soldati A. 2016. Turbulence modification by dispersion of large deformable droplets. *Eur. J. Mech. B* 55:294–99
Scarbolo L, Molin D, Perlekar P, Sbragaglia M, Soldati A, Toschi F. 2013. Unified framework for a side-by-side comparison of different multicomponent algorithms: Lattice Boltzmann versus phase field model. *J. Comput. Phys.* 234:263–79
Scarbolo L, Soldati A. 2013. Turbulence modulation across the interface of a large deformable drop. *J. Turbul.* 14:27–43
Scardovelli R, Zaleski S. 1999. Direct numerical simulation of free-surface and interfacial flow. *Annu. Rev. Fluid Mech.* 31:567–603
Shan X, Chen H. 1993. Lattice Boltzmann model for simulating flows with multiple phases and components. *Phys. Rev. E.* 47:1815–19
Shardt O, Derksen J, Mitra S. 2013. Simulations of droplet coalescence in simple shear flow. *Langmuir* 29:6201–12
Snyder M, Knio O, Katz J, Le Maître O. 2007. Statistical analysis of small bubble dynamics in isotropic turbulence. *Phys. Fluids* 19:065108
Spandan V, Lohse D, Verzicco R. 2016. Deformation and orientation statistics of neutrally buoyant sub-Kolmogorov ellipsoidal droplets in turbulent Taylor–Couette flow. *J. Fluid Mech.* 809:480–501
Spandan V, Meschini V, Ostilla-Mónico R, Lohse D, Querzoli G, et al. 2017a. A parallel interaction potential approach coupled with the immersed boundary method for fully resolved simulations of deformable interfaces and membranes. *J. Comput. Phys.* 348:567–90
Spandan V, Verzicco R, Lohse D. 2017b. Deformable ellipsoidal bubbles in Taylor-Couette flow with enhanced Euler-Lagrangian tracking. *Phys. Rev. Fluids* 2:104304
Spandan V, Verzicco R, Lohse D. 2018. Physical mechanisms governing drag reduction in turbulent Taylor-Couette flow with finite-size deformable bubbles. *J. Fluid Mech.* 849:R3
Sugiyama K, Calzavarini E, Lohse D. 2008. Microbubbly drag reduction in Taylor-Couette flow in the wavy vortex regime. *J. Fluid Mech.* 608:21–41
Sun Y, Beckermann C. 2007. Sharp interface tracking using the phase-field equation. *J. Comput. Phys.* 220:626–53
Sussman M, Puckett E. 2000. A coupled level set and volume-of-fluid method for computing 3D and axisymmetric incompressible two-phase flows. *J. Comput. Phys.* 162:301–37
Sussman M, Smereka P, Osher S. 1994. A level set approach for computing solutions to incompressible two-phase flow. *J. Comput. Phys.* 114:146–59
Swift M, Orlandini E, Osbornand WR, Yeomans JM. 1996. Lattice Boltzmann simulations of liquid-gas and binary fluid systems. *Phys. Rev. E* 54:5041–52
Tryggvason G, Bunner B, Esmaeeli A, Juric D, Al-Rawahi N, et al. 2001. A front-tracking method for the computations of multiphase flow. *J. Comput. Phys.* 169:708–59
Tryggvason G, Dabiri S, Aboulhasanzadeh B, Lu J. 2013. Multiscale considerations in direct numerical simulations of multiphase flows. *Phys. Fluids* 25:031302
Tryggvason G, Esmaeeli A, Lu J, Homma S, Biswas S. 2006. Recent progress in computational studies of disperse bubbly. *Multiph. Sci. Technol.* 18:231–49
Unverdi S, Tryggvason G. 1992. A front-tracking method of viscous incompressible, multi-fluid flows. *J. Comput. Phys.* 100:25–37
van der Veen R, Huisman S, Merbold S, Harlander U, Egbers C, et al. 2016. Taylor–Couette turbulence at radius ratio $\eta = 0.5$: scaling, flow structures and plumes. *J. Fluid Mech.* 799:334–51

Vanella M, Balaras E. 2009. A moving-least-squares reconstruction for embedded-boundary formulations. *J. Comput. Phys.* 228:6617–28

Wang LP, Maxey MR. 1993. The motion of microbubbles in a forced isotropic and homogeneous turbulence. *Appl. Sci. Res.* 51:291–96

Yue P, Zhou C, Feng J. 2007. Spontaneous shrinkage of drops and mass conservation in phase-field simulations. *J. Comput. Phys.* 223:1–9

Annual Review of
Fluid Mechanics

Volume 51, 2019

Contents

Indexes

Errata

An online log of corrections to *Annual Review of Fluid Mechanics* articles may be found at http://www.annualreviews.org/errata/fluid